

JGR Atmospheres

RESEARCH ARTICLE

10.1029/2019JD031955

Special Section:

Integrative Monsoon Frontal Rainfall Experiment

Key Points:

- The hydrometeor budget characteristics discussed based on two representative cases of Meiyu frontal rainstorms associated with different circulation patterns
- The major conversion pathways for raindrops relevant with the active ice-dependent cloud processes revealed in Meiyu frontal rainstorms
- The differences in the activity level of ice-dependent processes resulted from the different conditions dominated by the different circulation patterns

Correspondence to:

Y. Ding,
 yi.deng@eas.gatech.edu

Citation:

Li, C., Deng, Y., Cui, C., Wang, X., Dong, X., & Jiang, X. (2020). Hydrometeor budget of the Meiyu frontal rainstorms associated with two different atmospheric circulation patterns. *Journal of Geophysical Research: Atmospheres*, 125, e2019JD031955. <https://doi.org/10.1029/2019JD031955>

Received 31 OCT 2019

Accepted 4 JUL 2020

Accepted article online 29 JUL 2020

The copyright line for this article was changed on 19 SEP 2020 after original online publication.

©2020. American Geophysical Union.
 All Rights Reserved.

Hydrometeor Budget of the Meiyu Frontal Rainstorms Associated With Two Different Atmospheric Circulation Patterns

Chao Li¹ , Yi Deng² , Chunguang Cui¹, Xiaofang Wang¹ , Xiquan Dong³ , and Xingwen Jiang⁴ 

¹Hubei Key Laboratory for Heavy Rain Monitoring and Warning Research, Institute of Heavy Rain, China Meteorological Administration, Wuhan, China, ²School of Earth and Atmospheric Sciences, Georgia Institute of Technology, Atlanta, GA, USA, ³Department of Hydrology and Atmospheric Sciences, University of Arizona, Tucson, AZ, USA, ⁴Institute of Plateau Meteorology, China Meteorological Administration, Chengdu, China

Abstract Characteristics of hydrometeor budget and the microphysical processes responsible for heavy precipitation are studied based on the WRF model simulations of two representative Meiyu frontal rainstorms that are associated with two distinct atmospheric circulation patterns. Case 1 is characterized by the coupling of the Eastward Propagating Mesoscale Vortex (EPMV) and Meiyu front, while Case 2 is dominated by the interaction between the Low-Level Wind Shear (LLWS) and Meiyu front. The temporal and spatial characteristics of the hydrometeor budget are validated against observations and assimilation products including those obtained during the 2018 Integrative Monsoon Frontal Rainfall Experiment (IMFRE) campaign and discussed in the context of contrasting the precipitation intensification and dissipation stage. Specifically, the ice-dependent cloud processes, rather than the liquid-dependent cloud processes, are predominantly responsible for the variation of precipitation. These terms include the deposition from water vapor to the ice phase hydrometeors, the accretion from cloud liquid water to the ice phase hydrometeors in the upper troposphere, and the melting of the ice phase hydrometeors into raindrops in the mid-lower troposphere. Then three major ice cloud conversion pathways and two minor warm cloud conversion pathways for the formation of raindrops are extracted from the overall microphysical processes active in both Case 1 and Case 2. One of the key findings is that ice-dependent cloud processes are significantly more active in the case characterized by the coupling of EPMV and Meiyu front, and this difference is at least partly explained by the differences in dynamical and thermodynamic conditions dominated by the circulation patterns.

1. Introduction

During June and July in the summer of every year, a precipitation zone with a high probability for torrential rain occurs and lasts for approximately 2 to 3 weeks, its coverage ranges from the Mid-lower Reaches of the Yangtze River (MRYR) in China to Southwestern Japan. This phenomenon is called the “Meiyu” in China and the “Baiu” in Japan (Zhou et al., 2004). The powerful frontal system of Meiyu usually triggers heavy precipitation and causes widespread flooding (Tao, 1980), making it an important topic in the realm of scientific research. However, it is quite difficult to make accurate predictions of the extreme precipitation, since the complex precipitation mechanism, especially the cloud microphysical process, has not been revealed thoroughly. Previous research (Zhang et al., 2004) has confirmed that the Meiyu frontal rainstorms can be classified into three different types based on the atmospheric circulation pattern. The first type is triggered by meso- β Mesoscale Convective Systems (MCSs), the second type is triggered by the developing cyclones originating from the eastern slope of the Tibetan Plateau, and the third type is triggered by a deep trough located in the upper reaches of the Yangtze River in the higher troposphere, which accompanied by the low-level wind shear in the middle reaches of the Yangtze River in the lower troposphere. More attention should be paid to the last two types for its more frequent occurrence and higher probability to cause persistent and extreme precipitation in the MRYP during Meiyu period each year.

The cycling of energy, water, and chemical species through the Earth’s atmosphere is critically affected by the cloud microphysical processes (Grabowski et al., 2018), and the evolution of Meiyu frontal rainstorm

is not an exception. Previous investigations of the cloud microphysical processes relevant to the Meiyu front rainstorm have achieved some significant findings. In the late twentieth century, Kenneth and Liu (1990) systematically investigated the cloud microphysical processes of Meiyu front rainstorm and found that some aggregation is occurring during melting, and the interaction of coalescence and breakup are the prominent microphysical processes in the warm rain region. Coalescence typically dominates over breakup. But the two processes will approximately arrive at equilibrium when the precipitation reaches the Earth's surface. Thanks to the great advancements of the meteorological detection technology, detailed investigations of cloud microphysical processes in Meiyu rainstorms have become more viable. For instance, the relatively new video-sonde as a new detection equipment provides an excellent medium for investigating the properties of different hydrometeors within Meiyu rainstorms. The operation principle of the video-sonde is simply an induction ring which is used to measure the charge on falling particles with a video camera that records images of the particles. Takahashi et al. (2001) used the video-sonde data to discover the existence of many large graupel particles in a narrow area of the cloud just above the freezing level, and it is shown that the abundant accumulation of water near the melting layer is produced by the rapid growth of graupel through the capture of super cooled droplets transported from the merging cell. Further research showed that the heavy rainfall is produced by extensive growth of the graupel and frozen drops in the convective center near the melting level (Takahashi, 2006). Based on the joint detection of a video-sonde and a radiometer-sonde, Suzuki et al. (2014) discovered that the nearly spherical graupels and cone-like graupels coexist in the Meiyu clouds, and they originate both from frozen particles lifted by updrafts and ice crystals by accretion. Therefore, it is effectively proven with the in-situ observations that the variation of ice phase hydrometeors is an important part of microphysical processes and affects the subsequent precipitation. With the advancement of computational and numerical abilities in recent years, numerical modeling is now able to provide an alternative approach to study the intrinsic interconnection among different hydrometeors. Normura et al. (2012) used a cloud-resolving model to examine the impact of sedimentation of cloud ice on the precipitation intensity in various typical precipitation systems, including Baiu frontal systems. It is revealed that cloud ice concentrates at a lower level with sedimentation than that without sedimentation and converts to snow and graupel by microphysical growth processes. Idealized experiments reveal that the growth of drizzle droplets in the merging cells accelerates hail growth near the freezing level, and it plays a critical role in the accumulation of rainwater near the freezing level (Takahashi & Keenan, 2004). Water phase changes are remarkable in Meiyu frontal rainstorms because of the severe convection. Previous studies have confirmed that the melting process and evaporative cooling processes have profound impacts on the persistence of convection, and thus the evolution of different phase of hydrometeors is highly dependent on the lifespan and the microstructure of Meiyu frontal rainstorms (Fernandez et al., 2016).

A plenty of valuable discoveries relevant to cloud microphysical characteristics of Meiyu frontal rainstorms have been achieved and the close correlation between the cloud microphysical processes and the precipitation has also been confirmed. However, the issue concerning how the cloud microphysical processes within Meiyu frontal rainstorms regulating the evolution of precipitation needs further study for a deeper understanding of the complex precipitation mechanism. The analysis on the hydrometeor budget probably can give a clear answer to it. Hence, this paper makes an attempt to reveal this unknown issue based on two representative cases of Meiyu frontal rainstorms dominated by totally different atmospheric circulation patterns. The Case 1 characterized by the coupling between the Eastward Propagation Mesoscale Vortex (EPMV) and the Meiyu front occurred in the MRYR from 30th June to 2nd July in 2016, which could be categorized into the second type of Meiyu front rainstorm. The Case 2 dominated by the interaction between the Low-Level Wind Shear (LLWS) and the Meiyu front occurred in the western Hubei Province from 29th June to 30th June in 2018, and this case happens to be captured by the integrated observation from the Integrative Monsoon Frontal Rainfall Experiment (IMFRE) campaign. These two cases were selected out for not only their representativeness of the Meiyu frontal rainstorm, but also the more frequent occurrences of these two types of Meiyu frontal rainstorm in summer. Actually, the deficiencies of numerical models' prediction capabilities for these typical Meiyu frontal rainstorms lead to the failure to make timely and accurate predictions of extreme precipitation in some local areas. Thus, further investigations of these typical cases are in great demand to find out some distinctive features of cloud microphysical processes in Meiyu frontal rainstorms for improving the numerical model prediction capability of the heavy rainfall.

Table 1
The Settings of Physics Parameter for the WRF Simulation

Horizontal resolution	Grid number	Microphysics scheme	Longwave radiation scheme	Shortwave radiation scheme	Surface layer scheme	Land surface scheme	Boundary layer scheme
9 km	630 × 400	Milbrandt-Yau 2-moment scheme	RRTM scheme	Dudhia Scheme	Monin-Obukhov scheme	Thermal diffusion scheme	YSU scheme

2. Data Set and Methodology

The primary data applied in this paper consist of the following data sets: The Final Operational Global Analysis (FNL) data from NCEP with the temporal and spatial resolution of 6 hr and $1^\circ \times 1^\circ$, respectively; the brightness temperature (T_B) data retrieved from the FY (Fengyun)-2 series stationary satellite; the Climate Prediction Center Morphing Technique (CMORPH) hourly fusion precipitation data from the National Meteorological Information Center; the cloud reanalysis data from the Local Analysis and Prediction System (LAPS) with the temporal and spatial resolution of 1 hr interval and $1^\circ \times 1^\circ$, respectively. The CMORPH is a fusion data (hourly rain gauge data merged with satellite-based precipitation products). Since the accuracy of the gauge-based analysis relies on both density and configuration of the gauge network and the interpolation strategy, and satellite-based precipitation products that are generated by blending passive microwave (PMW) and infrared (IR) sensors are capable of detecting spatial patterns and temporal variations of precipitation at a finer resolution, which is particularly useful over poorly gauged regions, the improved data sets can better capture some varying features of hourly precipitation in heavy weather events (Shen et al., 2014). Besides, the LAPS developed by NOAA's Earth System Research Laboratory (ESRL) in Boulder, Colorado, combines a wide array of observed meteorological data sets (meteorological networks, radar, satellite, soundings, and aircraft) into a unified atmosphere analysis with a time interval of an hour or less (Hiemstra et al., 2006). The output products of the three-dimensional LAPS analyses include wind, temperature, radar reflectivity, moisture, and some cloud analysis products (Li et al., 2009). One of the unique features of the LAPS data includes combining data sources like surface observations, satellites, pilot reports, and radar data to provide a more complete three-dimensional view of clouds. And the quantities related with cloud parameters provided by LAPS include cloud liquid water, cloud ice, cloud snow, rain content, cloud base, cloud top, cloud type, cloud cover fraction, and so on (Albers et al., 1996).

The detailed parameters of the WRF model (including the adopted parameterization schemes) are shown in Table 1 (Dudhia, 1989; Hong et al., 2006; Jimenez & Dudhia, 2012; Milbrandt & Yau, 2005b; Mlawer et al., 1997). Considering that the microphysics scheme plays a key role in the simulation of each category of hydrometeors, the Milbrandt2 scheme is adopted due to the following reasons. It is commonly known that many bulk schemes represent the size spectra of each precipitating hydrometeor category by a three-parameter gamma distribution function of the form

$$N(D) = N_0 D^\alpha e^{-\lambda D},$$

where D represents the effective diameter, N represents the total number concentration per unit volume of particles, N_0 is a constant parameter, α is the dispersion parameter, and λ is the slope parameter. Milbrandt and Yau (2005b) introduced a two-moment bulk microphysics parameterization consisting of six distinct hydrometeor types (two liquid and four ice phase categories) with each type represented by the above gamma size distribution function, and the dispersion parameter α is set as a fixed value in this new bulk scheme. Different from other schemes, the Milbrandt scheme has predominance in the simulation of heavy rainstorm with severe convection, especially hail events (Milbrandt & Yau, 2006; Morrison & Milbrandt, 2011). Coincidentally, the EPMV type and LLWS type of Meiyu frontal rainstorms are both prone to produce severe convection, and the simulation superiority for severe convection determines that the Milbrandt scheme may be more suitable for the budget analysis of hydrometeors in Meiyu frontal rainstorms.

As stated above, the Milbrandt2 scheme classifies the cloud hydrometeors into six different species, plus one species of gas-phase hydrometeors: water vapor (Q_v), cloud liquid water (Q_c), rain water (Q_r), cloud ice (Q_i), snow (Q_s), graupel (Q_g), hail (Q_h). Figure 1 explicitly shows the schematics for the ice and warm cloud

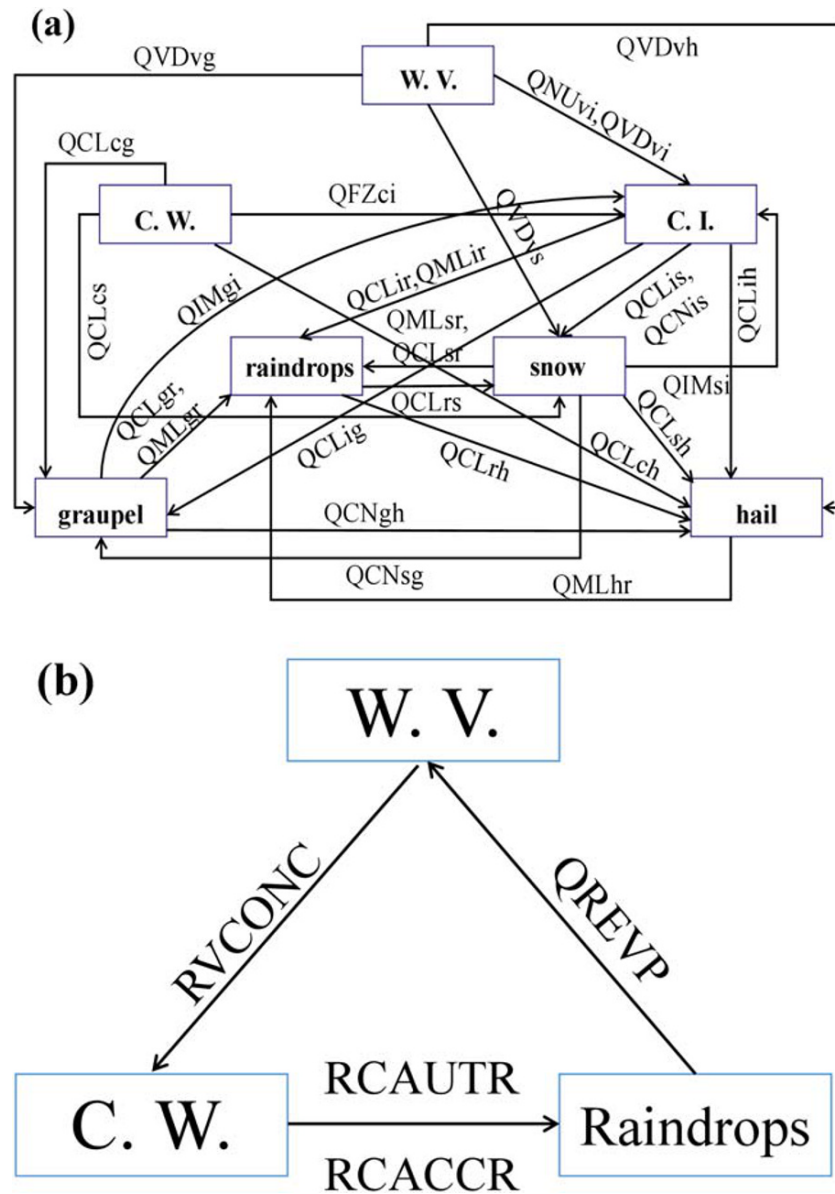


Figure 1. The schematics diagram of the cloud microphysical processes ((a) ice cloud processes, (b) warm cloud processes) among different species of hydrometeor (the arrows represent the conversion direction among different hydrometeors, the character of W.V. represents water vapor, the character of C.W. represents cloud water, the character of C.I. represents cloud ice).

microphysical processes among these hydrometeors incorporated in the Milbrandt2 microphysics scheme within WRF 3.9 version (Milbrandt & Yau, 2005a). The source and sink terms of the mixing ratios concerning each species of hydrometeors are listed below (Milbrandt & Yau, 2005b).

Ice cloud microphysical processes:

$$S_{Qv} = -QNUvi - QVDvi - QVDvs - QVDvg - QVDvh - RVCONC, \quad (1)$$

$$S_{Qi} = QNUvi + QVDvi + QFZci - QCNis - QCLir - QCLis - QCLig - QMLir - QCLih + QIMsi + QIMgi, \quad (2)$$

$$S_{Qc} = -QCLcs - QCLcg - QCLch - QFZci, \quad (3)$$

Table 2
The Notations of Each Term in the Tendency Equations

Notations	Microphysical process	Notations	Microphysical process
QCLch	Accretion from cloud liquid water to hail	QIMsi	Rime growth from snow to cloud ice
QCLcg	Accretion from cloud liquid water to graupel	QHwet	Humidification physical process
QCLcs	Accretion from cloud liquid water to snow	QMLir	Melting of cloud ice into raindrops
QCLig	Accretion from cloud ice to graupel	QMLgr	Melting of graupel into raindrops
QCLih	Accretion from cloud ice to hail	QMLhr	Melting of hail into raindrops
QCLis	Accretion from cloud ice to snow	QMLsr	Melting of snow into raindrops
QCLir	Accretion from cloud ice to raindrops	QNUvi	nucleation from vapor to cloud ice
QCLgr	Accretion from graupel to raindrops	QREVP	Evaporation of raindrops to vapor
QCLri	Accretion from raindrops to ice	QSHhr	Shedding from hail to raindrops
QCLrg	Accretion from raindrops to graupel	QVDvi	Deposition from vapor to cloud ice
QCLrh	Accretion from raindrops to hail	QVDvg	Deposition from vapor to graupel
QCLrs	Accretion from raindrops to snow	QVDvh	Deposition from vapor to hail
QCNis	Auto conversion from cloud ice to snow	QVDvs	Deposition from vapor to snow
QCNgh	Auto conversion from graupel to hail	RCAUTR	Auto conversion from cloud liquid water to raindrops
QCNsg	Auto conversion from snow to graupel	RCACCR	Accretion from cloud liquid water to raindrops
QFzci	Freezing from cloud liquid water into cloud ice	RVCONC	Condensation/evaporation from vapor to cloud liquid water
QFZrh	Freezing from raindrops into hail	Sedi_Qx	Sedimentation of raindrops, cloud ice, snow, graupel, hail
QIMgi	rime growth from graupel to cloud ice		

$$S_{Qs} = QCNis + QVDvs + QCLcs - QCNsg - QMLsr - QIMsi - QCLsr + QCLis - QCLsh + Dsrs*(QCLrs + QCLsr), \quad (4)$$

$$S_{Qs} = QCNsg + QVDvg + QCLcg - QCLgr - QMLgr - QCNgh - QIMgi + QCLig + Dirg*(QCLri + QCLir) + Dgrg*(QCLrg + QCLgr) + Dsrg*(QCLrs + QCLsr), \quad (5)$$

$$S_{Qh} = Dirh*(QCLri + QCLir) - QMLhr + QVDvh + QCLch + Dsrh*(QCLrs + QCLsr) + QCLih + QCLsh + QFZrh + QCLrh + QCNgh + Dgrh*(QCLrg + QCLgr), \quad (6)$$

$$S_{Qr} = -QCLri + QMLsr - QCLrs - QCLrg + QMLgr - QCLrh + QMLhr - QFZrh + QMLir + QCLsr + QCLgr. \quad (7)$$

Warm cloud microphysical processes:

$$S_{Qc} = -RCAUTR - RCACCR + RVCONC, \quad (8)$$

$$S_{Qr} = -QREVP + RCAUTR + RCACCR. \quad (9)$$

The tendency equations listed above contain the primary microphysical process, and the interpretation of the notations of each term in these equations are listed in Table 2. The hydrometeor budget characteristics are achieved by analyzing the evolution of different hydrometeors and their corresponding source and sink terms during the persistence of a Meiyu frontal rainstorm.

3. Assessment of the Performance of the Adapted Microphysics Scheme

Due to the uncertainties of microphysics scheme in WRF, the assessment of the model simulation performance is necessary. Since the LAPS data can provide high temporal and spatial resolution cloud analysis products, in addition, the accuracy and credibility of the LAPS system has been verified extensively (Albers et al., 1996; Birkenheuer, 1999, 2001; Hiemstra et al., 2006; Jiang et al., 2015), thus to a certain extent, the microscopic parameters related with different hydrometeors derived from LAPS can be regarded as the semiobservation to assess the simulation performance of the sensitivity tests applied with different prevailing microphysics schemes (i.e., Milbrandt, Morrison, SBU, Thompson). Considering the simulation of the cumulative precipitation is one of the most effective criteria to judge the simulation capacity of different microphysics schemes, and Figure 2 clearly demonstrates that the Milbrandt scheme and the Thompson scheme have slightly better simulation performances of the cumulative precipitation than other schemes. The simulation of different hydrometeors is another effective measure to judge the simulation

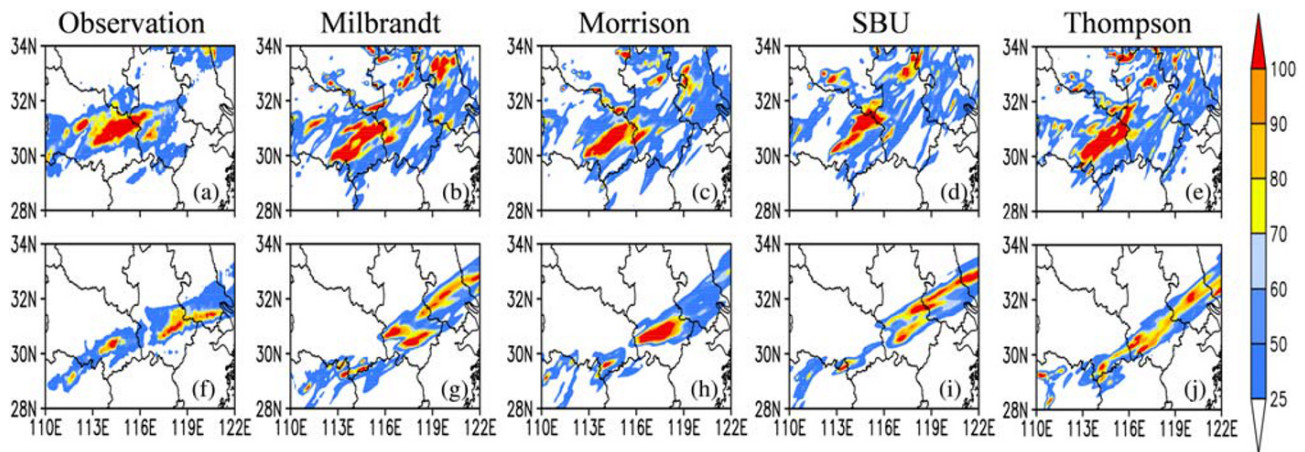


Figure 2. The observation ((a) and (f) for CMORPH) and the sensitivity test of the cumulative precipitation ((a) to (e) denote the intensification stage from 12 o'clock on 30 June to 0 o'clock on 1 July, (f) to (j) denote the dissipation stage from 12 o'clock on 1 July to 0 o'clock on 2 July, the shaded color represents the cumulative precipitation, unit: mm) based on different microphysics schemes ((b) and (g) for Milbrandt, (c) and (h) for Morrison, (d) and (i) for SBU, (e) and (j) for Thompson).

performance, however, since the classification threshold of each species of hydrometeors in different schemes differs remarkably, it can result in the discrepancies of the cloud region identified by the mixing ratio of cloud ice or cloud water exceeding certain value output from different schemes definitely. Therefore, a new definition of cloud region is proposed for scientific contrast, which adapts the similar criterion that defined in the reference published by Xu (1995). To be specific, if the totality of all different species of hydrometeor path exceeds the threshold (i.e., 0.005 kg/m^2), the grid is regarded as covered by cloud, the cloud region is composed of all cloud-covered grid. Figure 3 clearly demonstrated the cloud region identified by different schemes during different period. The result shows that the Milbrandt

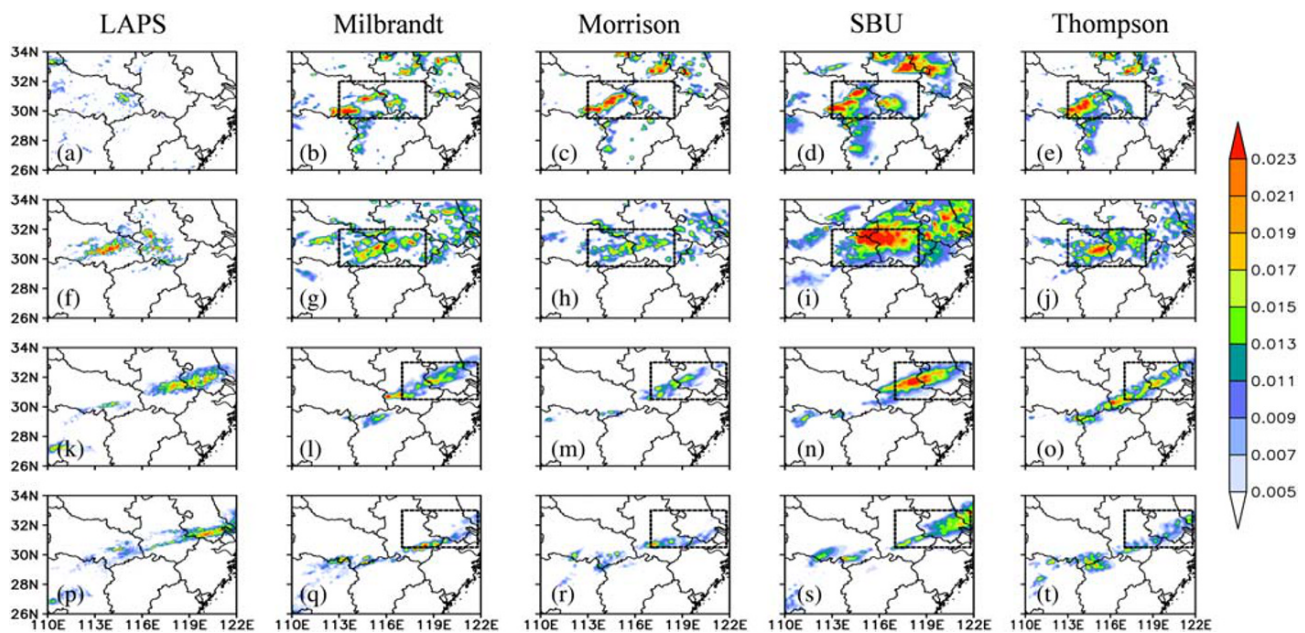


Figure 3. The observation ((a), (f), (k), (p) for LAPS) and the sensitivity test of the cloud region ((a) to (e) denote the period from 12 o'clock on 30 June to 18 o'clock on 30 June, (f) to (j) denote the period from 18 o'clock on 30 June to 0 o'clock on 1 July, (k) to (o) denote the period from 12 o'clock on 1 July to 18 o'clock on 1 July, (p) to (t) denote the period from 18 o'clock on 1 July to 0 o'clock on 2 July, the shaded color represent the total path of cloud liquid water and cloud ice, unit: kg/m^2) based on different microphysics schemes ((b), (g), (l), (q) for Milbrandt; (c), (h), (m), (r) for Morrison; (d), (i), (n), (s) for SBU; (e), (j), (o), (t) for Thompson).

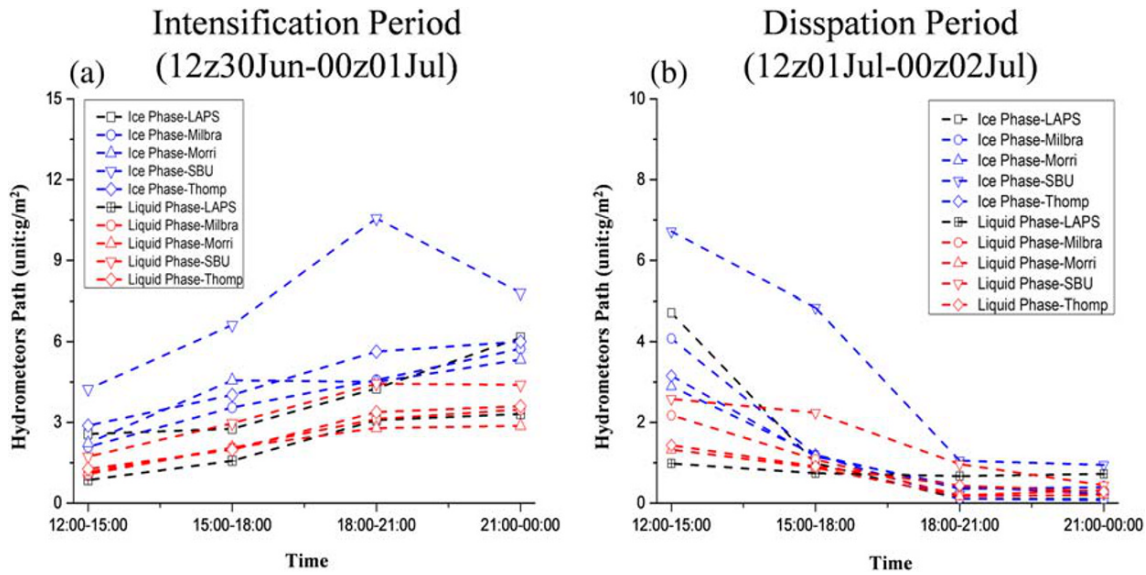


Figure 4. The variation of the spatiotemporal averaged (the time span for averaging is set 6 hr in length, the space range for averaging is limited within the specified region marked with black dotted lines in Figure 3) cloud ice path (blue dotted lines, unit: kg/m^2) and cloud liquid water path (red dotted lines, unit: kg/m^2) based on the control test (LAPS observation, black dotted lines, unit: kg/m^2) and the sensitivity tests (applied with Milbrandt, Morrison, SBU, Thompson scheme, respectively).

scheme and Morrison scheme have better simulation capacity of cloud region by contrast to the LAPS observation. Additionally, Figure 4 shows the variation of cloud ice path and cloud liquid water path derived from the LAPS observation and the sensitivity tests. The result further confirms the simulation superiority of Milbrandt scheme, that is, in the intensification period, the SBU scheme has the most remarkable deviation of simulation due to its obvious overestimation of both ice and liquid phase hydrometeors, while the Milbrandt scheme has the smaller simulation deviation of both ice and liquid phase hydrometeors than the Morrison scheme and the Thompson scheme. In the dissipation period, the remarkable overestimation of both ice phase and liquid phase hydrometeors still occurs in the simulation of SBU scheme, while the rest of schemes have better simulation performances, specially the Milbrandt scheme has the smallest deviation in simulating the variation of the ice phase hydrometeors among the whole schemes, despite of its slightly larger simulation deviation of liquid phase at the beginning of period. Based on the overall assessment of the simulation performances of all microphysics scheme, it is revealed that the Milbrandt scheme did show simulation superiority than other schemes in Meiyu frontal rainstorms, thus the Milbrandt scheme is naturally adopted in the budget analysis of hydrometeors.

4. Case Study Background

4.1. The Variations of Background Atmospheric Circulation and Cloud T_B

Both of the two selected cases of Meiyu frontal rainstorms caused severe flooding damages within the MRYS in the summer of 2016 and 2018, respectively. The background atmospheric circulation for Case 1 ((a-1) to (h-1) in Figure 5) shows that an EPMV originated from the eastern slope of Tibetan Plateau (TP), then moved eastward along the Yangtze River, and coupled with the Meiyu front within the MRYS subsequently, which brought a series of heavy precipitation consequently. The background atmospheric circulation of Case 2 ((a-2) to (h-2) in Figure 5) shows that an LLWS appeared in the western Hubei Province at first, then a subscale cyclonic vortex split off from the northeast of LLWS and continued to move northeastward, however, the LLWS still sustained in the western Hubei Province, and continuously interact with the Meiyu front in the MRYS, which also brought a series of heavy precipitation as well. The variations of cloud T_B (Brightness Temperature) shown in Figure 6 clearly demonstrate that the clouds intensified first and dissipated later, which shared synchronize change with the precipitation. Moreover, the reinforcement of

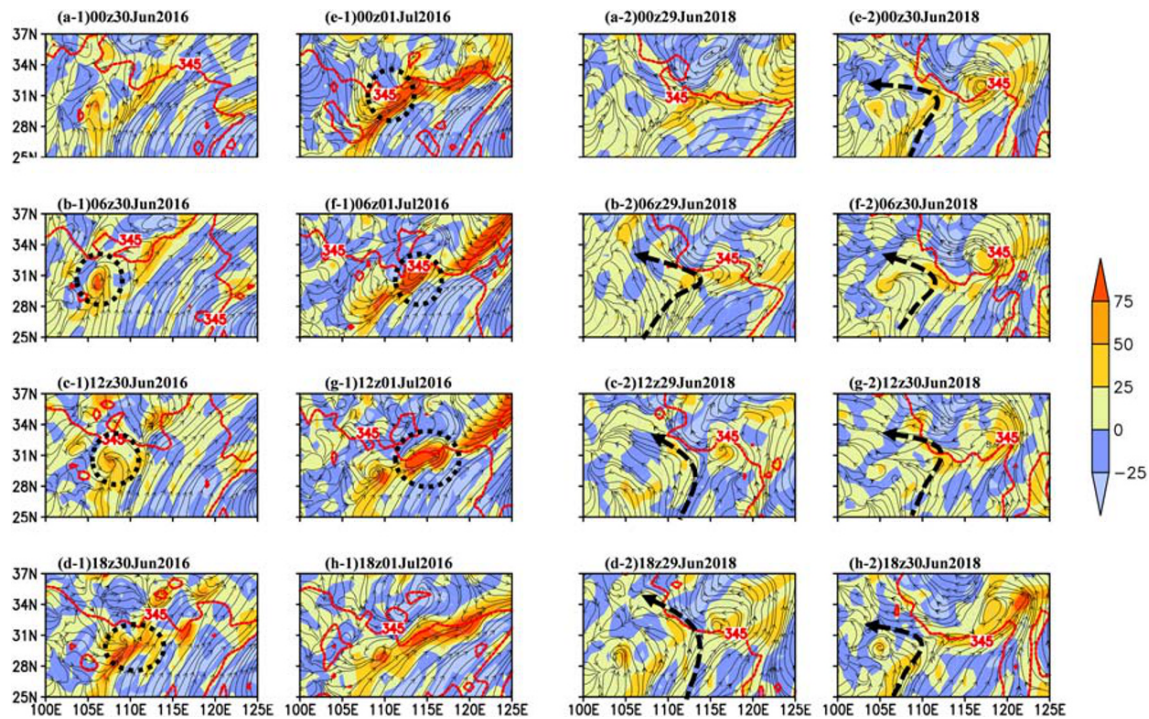


Figure 5. The background atmospheric circulation (black stream lines, $m*s^{-1}$) and the vertical vorticity (shaded, 10^5*s^{-1}) at 700 hPa isobaric surface for Case 1 ((a-1) to (h-1)) and Case 2 ((a-2) to (h-2)) (the red solid line denotes the Meiyu front that is marked in the 345 K isoline of the pseudo-equivalent potential temperature at 500 hPa isobaric surface, the ellipses marked with black dotted lines denote cyclonic vortex, and the curved arrows marked with black dotted lines denote the wind shear).

clouds in Case 1 was highly dependent on the coupling between the EMPV and the Meiyu front, while the reinforcement of clouds in Case 2 was mainly dependent on the interaction between the LLWS and the Meiyu front (the Meiyu front in the two both cases are denoted by the red dotted line that represents the 345 K isoline of pseudo-equivalent potential temperature, Zhang & Zhang, 2012, in the Figure 5).

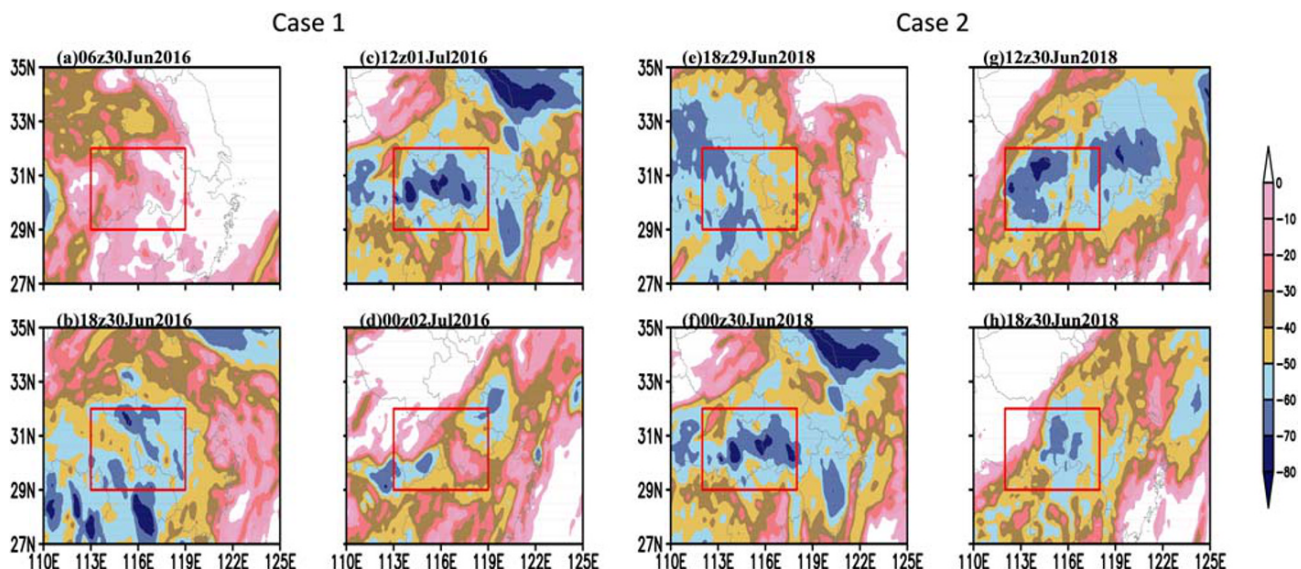


Figure 6. The cloud top brightness temperature (i.e., T_B , shaded color, unit: $^{\circ}C$) for Case 1 ((a) to (d)) and Case 2((e) to (h)) (the red rectangles denote the regions where the cloud clusters had remarkable change).

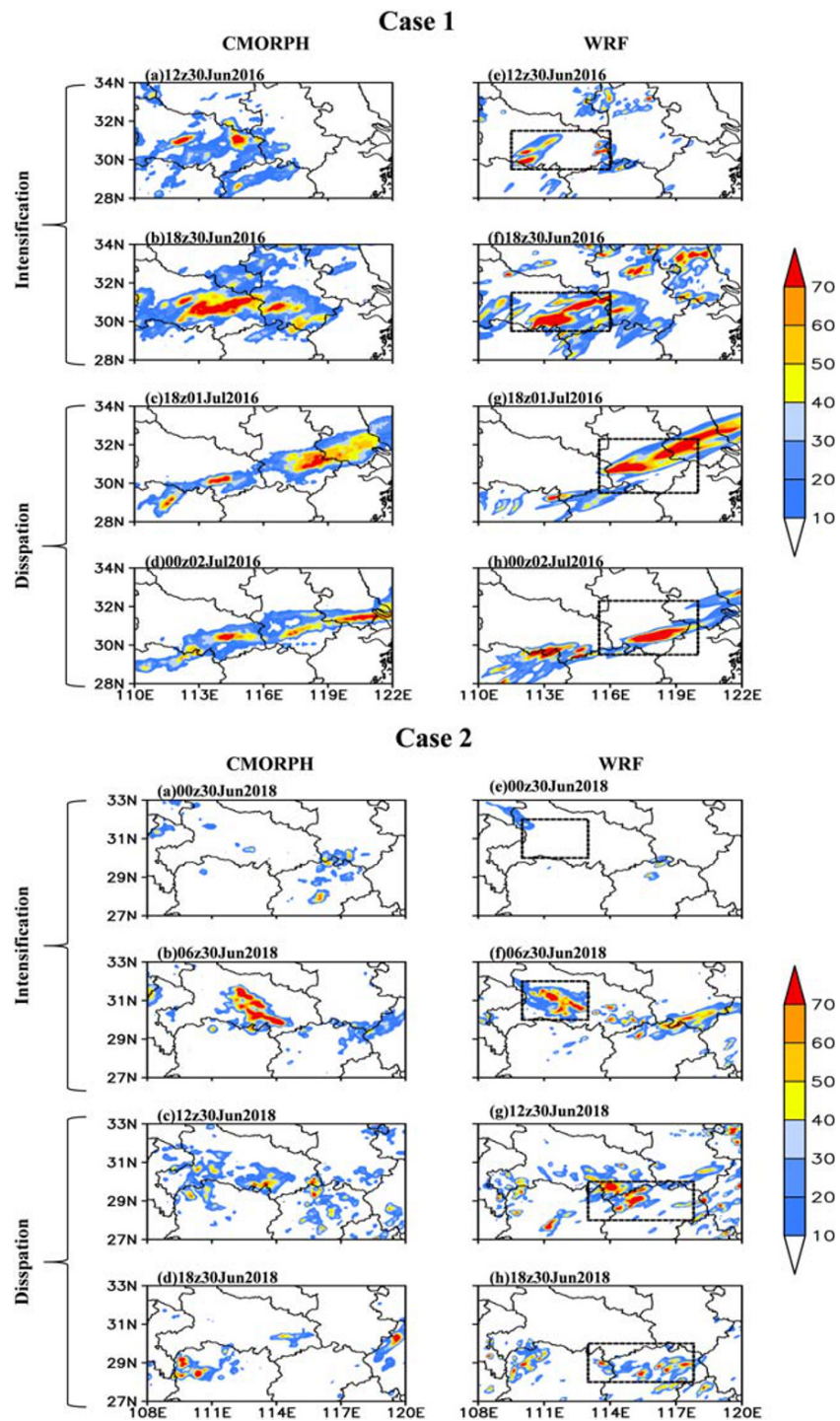


Figure 7. The contrast of the accumulated surface precipitation (shaded color, unit: mm) within 6 hr between CMORPH observation (a–d) and WRF simulation (e–h) for Case 1 (top) and Case 2 (bottom) (Dotted rectangle box represents the heavy rainfall area specified for the average calculation in the following analysis).

4.2. The Variation of the Precipitation

A detailed contrast of the precipitation between the simulation of WRF and the observation from CMORPH is presented in Figure 7. The comparison period is mainly focused in the enhancement of precipitation (defined as the intensification stage) and the weakening of precipitation (defined as the dissipation stage).

In Case 1, the time span of the intensification stage is set from 06z30Jun to 18z30Jun, and the dissipation stage is from 12z01Jul to 00z02Jul. In Case 2, the time span of the intensification stage and the dissipation stage are set from 18z29Jun to 06z30Jun and from 06z30Jun to 18z30Jun, respectively. The contrast results show that the WRF results have a roughly accurate reflection of heavy precipitation for both Case 1 and Case 2 in the overall, despite the false and omitted simulation in some local areas. Anyhow, the simulation bias is still in the normal range, thus it is feasible to apply the simulation results in the following hydrometeor budget analysis.

5. Results

5.1. The Vertical Distribution of Different Hydrometeors and Their Associated Budget Terms

Since different species of hydrometeors and their associated budget items have different vertical distribution characteristics, further analysis on it helps to reveal more correlation between the cloud microphysical processes and the heavy precipitation. Considering the opposite temporal tendency of precipitation intensity in the intensification stage and the dissipation stage, a contrast of the hydrometeor budget between the two stages will help to highlight the hydrometeor budget characteristics.

The time span for calculating the temporal average mixing ratio is set as 6 hr (i.e., the time interval of the output of the simulation results), and the spatial range for computing the spatial-averaged mixing ratio is set as the area where the cumulative precipitation exceeds over 10 mm/6 hr, then the time and regional-averaged mixing ratio of each species of hydrometeors and their associated budget items are shown in Figures 8 (Case 1) and 9 (Case 2). As shown in Figure 8, the time and regional-averaged mixing ratio of cloud ice presents an increasing tendency, in spite of its relatively small amount compared to the other hydrometeors. The source and sink terms are both distributed in the upper troposphere (above 400 hPa). Moreover, the QVDvi term contributes most to the growth of cloud ice, while the QCNi term contributes most to the consumption of it. This means that the deposition from water vapor to cloud ice (QVDvi) and the auto conversion from cloud ice to snow (QCNi) are the dominant microphysical processes. The condensation from water vapor to cloud water (RVCONC) classified into the warm cloud processes is the only source term of cloud water, which compensates for the consumption of cloud water. The others are all sink terms of cloud water that can be associated with ice cloud processes and warm cloud processes. And further analysis reveals that the budget terms related with ice cloud processes contribute more than those ones related with warm cloud processes for the consumption of cloud liquid water. Moreover, among those ones related with ice cloud processes, the QCLcg (cloud liquid water accreting with graupel) term contributes most to the consumption of cloud liquid water in the middle and upper troposphere (600 to 300 hPa). This means that the accretion from cloud liquid water to graupel (QCLcg) is the dominant microphysical process which influences the mixing ratio of cloud water. Different from cloud ice, the source and sink terms of the other ice phase hydrometeors (graupel, snow, hail) are distributed in lower levels of the troposphere (below 200 hPa). That is to say, the QCLcg term contributes most to the growth, while the QMLgr (graupel melting to raindrops) and QCNgh (graupel auto conversing to hail) terms contribute most to the consumption of graupel. Then the QCNgh (graupel auto converting to hail) term contributes most to the growth of hail, while QMLhr (hail melting to rain) term contributes most to the consumption of hail. Finally, the QVDvs (water vapor deposition to snow) and the QMLsr (snow melting to rain) terms contribute most to the growth and consumption of snow, respectively. Since the mixing ratio of raindrops is directly related to the precipitation intensity, it is revealed that the level of activity of the melting of these ice phase hydrometeors (graupel, snow, hail, cloud ice) directly dominates the precipitation intensity, since the melting of these ice phase hydrometeors contribute much more to the formation of raindrops, when these ones are compared to those warm cloud processes conversing cloud liquid water to raindrops directly.

In Case 2 (as shown in Figure 9), similar characteristics regarding the vertical distribution of each species of hydrometeors and their associated budget items can be found in both the intensification stage and the dissipation stage. However, the discrepancies are also significant, in particular to the melting of different species of ice phase hydrometeors to the formation of raindrops. The melting of snow contributes most to the formation of raindrops in the intensification stage for Case 2, while the melting of graupel contributes a little more

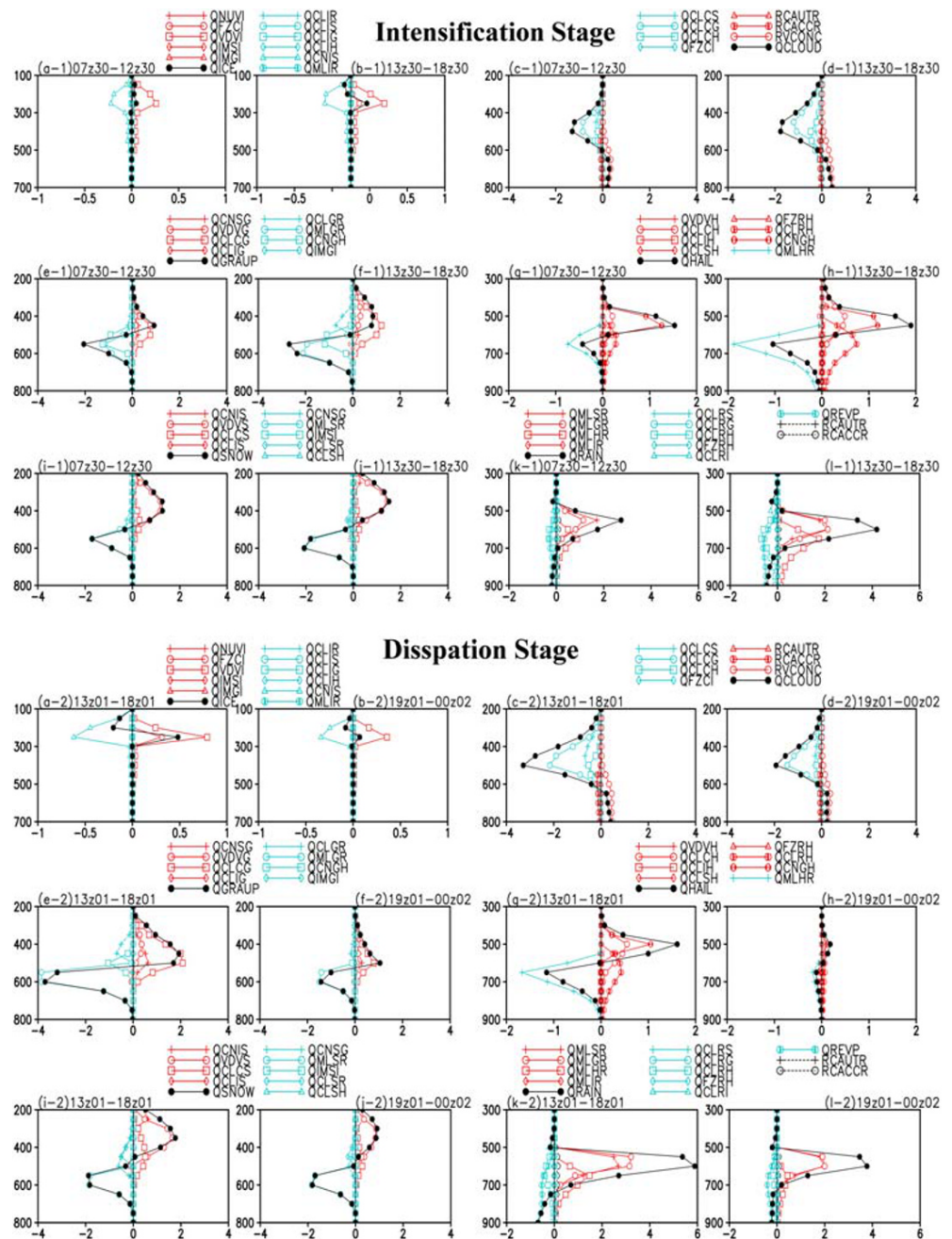


Figure 8. The vertical distribution (y axis denotes height, unit: hPa) of different species of hydrometeors ((a) and (b) denote cloud ice, (c) and (d) denote cloud liquid water, (e) and (f) denote graupel, (g) and (h) denote hail, (i) and (j) denote snow, (k) and (l) denote raindrops) and their associated budget terms (x axis denotes the relative change of the temporal-averaged mixing ratio of the hydrometeors and their associated budget terms, unit: $10^{-6} \text{ kg}/(\text{kg} \cdot \text{h})$) in the intensification stage (top) and the dissipation stage (bottom) for Case 1.

than snow to the formation of raindrops in the intensification stage for Case 1. Besides more differences are revealed by further contrast between the intensification stage and the dissipation stage for both Case 1 and Case 2. First, each species of hydrometeors and their associated budget terms share the similar tendencies with the variation of precipitation intensity, i.e., the vertical distribution of the regional-averaged mixing ratio of hydrometeors and their associated budget terms presents significant increase and decrease in the intensification and dissipation stage, respectively. Additionally, the ranking of the melting processes of the

5.2. The Temporal Variation of the Dominant Budget Terms

The dominant budget terms (selected out based on the relative contribution to the formation of the relevant hydrometeors) associated with each species of hydrometeors can be briefly classified into four primary groups based on the microphysical mechanism: the deposition from water vapor to ice phase hydrometeors (i.e., cloud ice, graupel, hail, and snow), the auto conversion among different ice phase hydrometeors (i.e., cloud ice, graupel, hail, and snow), the accretion from cloud liquid water to ice phase hydrometeors, and the melting of ice phase hydrometeors into raindrops.

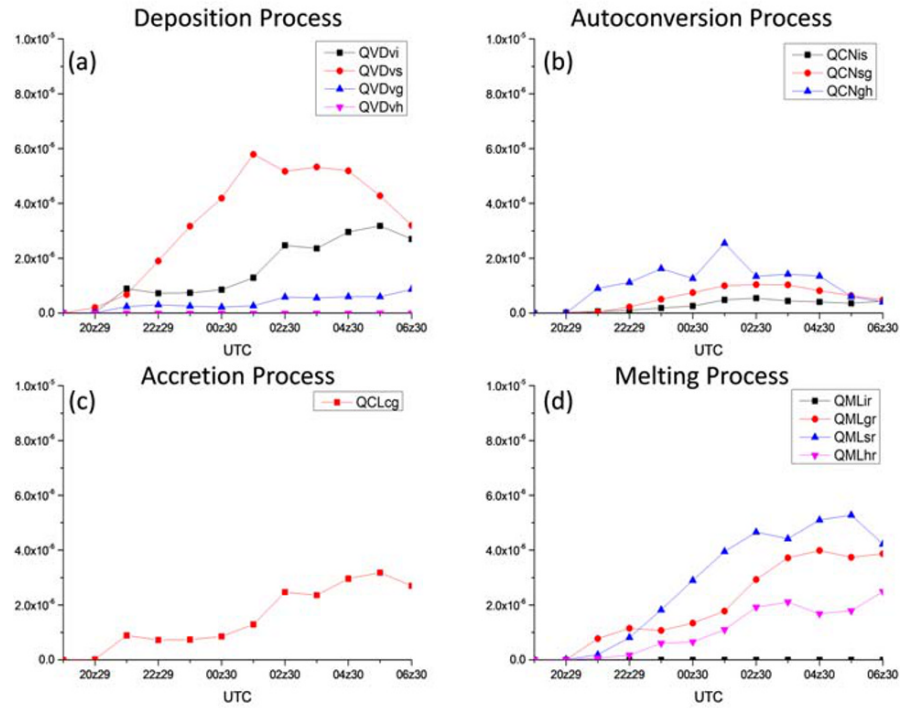
Figure 10 shows the temporal variation of different groups of the dominant budget terms in the development and the dissipation stage for Case 1. In the intensification stage (Figures 10a–10d), the QVDvs term increased the most significantly among all of the deposition processes. And the QCNgh term has the most significant change among the auto conversion processes. However, the first ranking budget terms in the group of the melting processes are not invariant. That is to say, the QMLsr term contributes most in early period, while the QMLhr and QMLgr terms contribute more to the melting processes than QMLsr in later period. Further investigation of intrinsic causes revealed that the reinforcement of deposition from water vapor to snow accelerates the melting from snow to raindrops in the early period, and the weakening of deposition from water vapor to snow reduces the melting from snow to raindrops in the later period. Although the deposition from water vapor to graupel is weaker in the later period, the increasing mixing ratio of graupel resulting from the reinforcement of accretion from cloud liquid water to graupel (i.e., QCLcg shown in Figure 10c) still promotes the melting of graupel into raindrops. Another considerable conversion pathway is the reinforcement of the melting of hail into raindrops, which is accelerated by the auto conversion from graupel to hail. In the dissipation stage (Figures 10e–10h), the deposition process is dominated by a significant decrease in the QVDvs term. Subsequently, the auto conversion process is weak and negligible in the dissipation stage. Moreover, a sharp decrease of the QCLcg, QMLsr, QMLgr, and QMLhr terms continues throughout the entire dissipation stage. The weakening of these microphysical processes are entirely responsible for the reduction of the precipitation intensity. One is the decrease in both the deposition from vapor to snow (QVDvs) and the accretion from cloud liquid water to graupel (QCLcg), which lead to the decrease of the subsequent melting processes (QMLsr and QMLgr). The second one is the constant consumption of hail without further replenishment results in a decrease of the mixing ratio of hail, which suppresses the subsequent melting process (QMLhr) correspondingly.

Figure 11 shows the temporal variation of different groups of the dominant budget terms in the development and the dissipation stage for Case 2. Numerous similarities concerning the variation of the dominant budget terms are found in Case 2, while the significant differences between Case 1 and Case 2 lie in the melting process in the intensification stage and the dissipation stage. In other words, in the intensification stage, since the deposition process from the vapor to the snow (QVDvs) in Case 2 is a little stronger than that in Case 1, and the accretion process from the cloud liquid water to the graupel (QCLcg) in Case 2 is notably weaker than that one in Case 1, both of these two aspects result in the melting of snow contributing most to the formation of raindrops in Case 2 in the whole intensification stage nearly, which determines the melting of ice phase hydrometeors processes are significantly different between Case 1 and Case 2. Moreover, in the dissipation stage, the reinforcement of the accretion processes from cloud liquid water to graupel (QCLcg) leads to the melting of graupel being the most contributory processes to the formation of raindrops rather than snow, which is consistent with Case 1.

5.3. The Conversion Pathway for the Formation of the Raindrops

Analysis has been done to reveal the budget characteristics of each species of hydrometeors in the intensification stage and the dissipation stage for both Case 1 and Case 2. Further investigation of the microphysical “flowchart” is useful in order to have an intuitive understanding of the correlation between the microphysical processes and the heavy precipitation. Since Case 1 and Case 2 both belong to the type of the Meiyu frontal rainstorms, they share numerous similar characteristics concerning the variation of hydrometeor budget. Figure 12 presents the microphysical flowchart diagnosed from the WRF results targeted for Case 1 and Case 2. The red and green arrows in the figures denote the increasing and the decreasing tendency, respectively. The first largest and second largest magnitude order of budget terms for each species of hydrometeor are selected out and presented in the microphysical flowchart. Overall speaking, the temporal tendencies of each species of hydrometeors share the same trend with the precipitation for both Case 1 and

Intensification Stage



Dissipation Stage

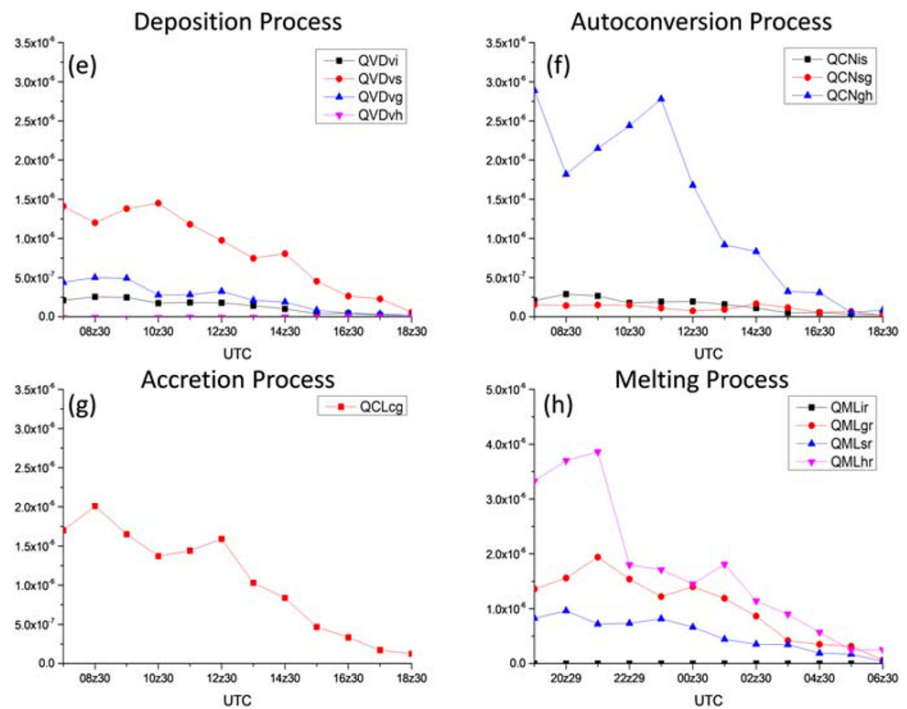
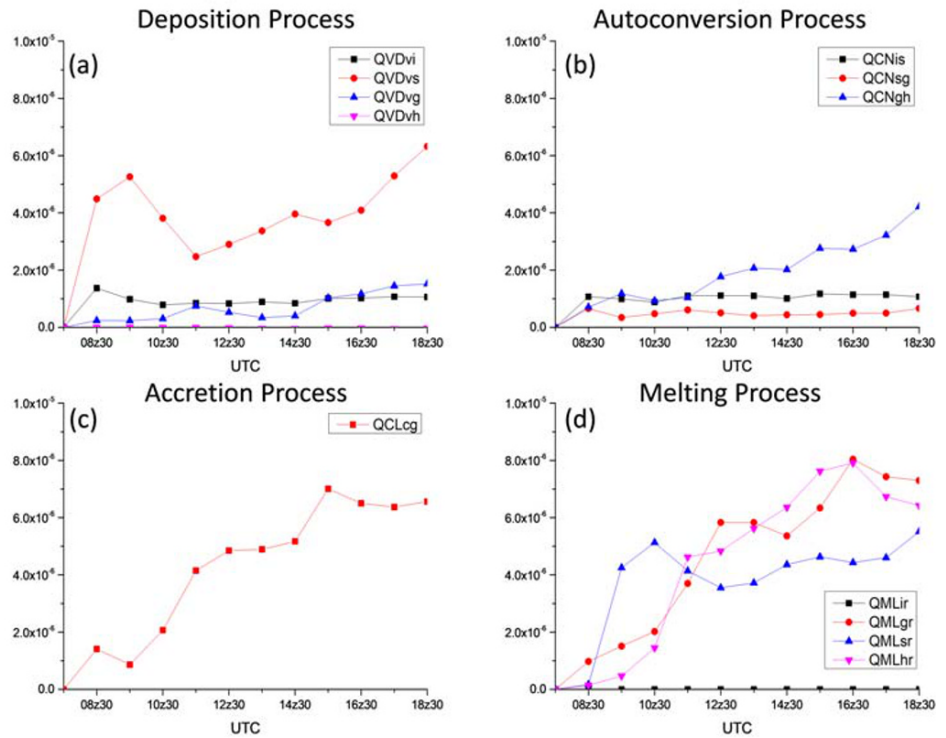


Figure 10. The temporal variation of the dominant microphysical processes ((a) and (e) denote the deposition process; (b) and (f) denote the autoconversion process; (c) and (g) denote the accretion process; (d) and (h) denote the melting process) in the intensification stage (top) and the dissipation stage (bottom) for Case 1 (the x axis represents time, the y axis represents regional-averaged hydrometeors path, unit: kg/m^3).

Intensification Stage



Dissipation Stage

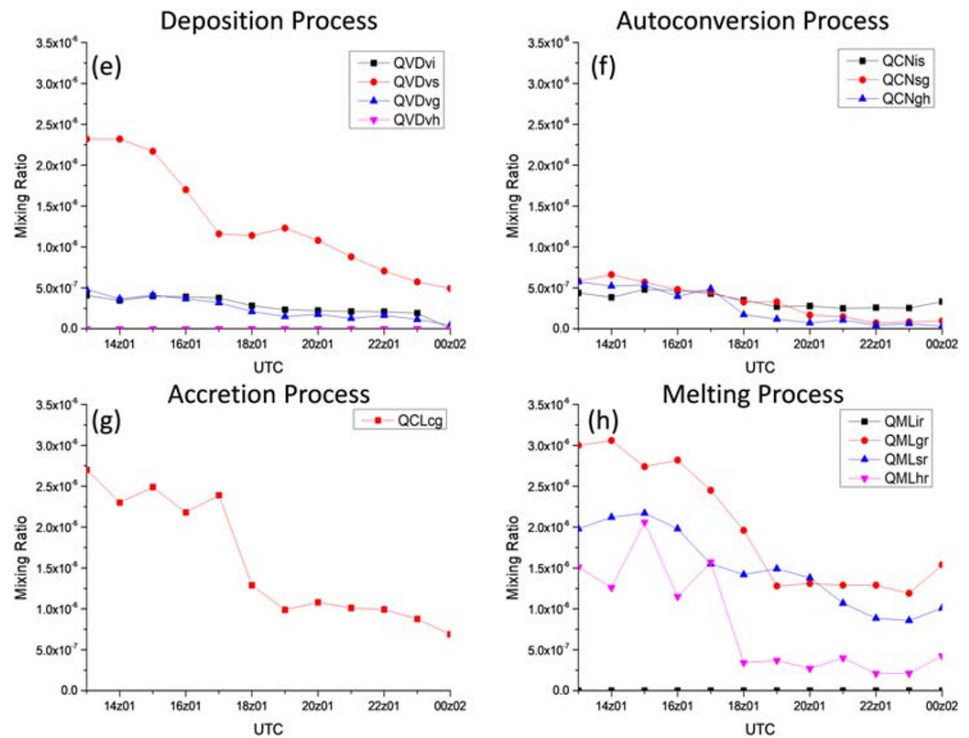


Figure 11. As in Figure 10, but for Case 2.

Case 2. Then three major routes of ice-dependent microphysical processes and two minor routes of liquid-dependent microphysical processes targeted for the formation of raindrops (shown in Figure 13) are extracted from the microphysical flowchart. In terms with those routes related with the ice-dependent microphysical processes, the first one begins with the deposition from water vapor to cloud ice first, followed by auto converting to graupel, and finally melting into raindrops; then the second one is the deposition from water vapor to graupel followed by melting into raindrops; and the third one is the accretion from cloud liquid water to snow followed by melting into raindrops. And in terms with those routes related with the liquid-dependent microphysical processes, it is revealed that the raindrops can be formed by the auto conversion or the accretion of cloud water particles directly. The ice-dependent microphysical processes can be regarded as the constitution of the ice cloud microphysical processes, which formed ice phase of hydrometeors in the upper troposphere and then melting into liquid phase in lower level of troposphere roughly, and the liquid-dependent microphysical processes can be regarded as the constitution of the warm cloud microphysical processes, which do not incorporate any ice phase change processes. The distinction in the magnitude order of the dominant budget terms associated with ice and warm microphysical processes (shown in Figure 12) indicates that those ice-dependent microphysical processes are more significant than those liquid-dependent microphysical processes for the formation of raindrops. But nonetheless, the role of QREVP (classified into the category of warm cloud processes) that compensates for the consumption of water vapor for the condensation processes is still prominent based on its magnitude order shown in the flowchart. What's more, most of the ice-dependent cloud processes in the intensification stage is stronger than that one in the dissipation stage, compared to the opposite tendency that the liquid-dependent cloud processes in the intensification stage are weaker than that one in the dissipation stage for the both two cases. Additionally, whether for Case 1 or Case 2, the temporal variation of the sedimentation flux of raindrops shown in Figure 14 shares a rather similar variation tendency with the precipitation, which links those ice-dependent cloud processes with the heavy rainfall tightly. In other words, the sedimentation process of raindrops effectively measures how much raindrops fall down on the ground and thus it builds a connection between the raindrops produced in the air and the precipitation on the ground, and the hydrometeor budget analysis has confirmed that the ice-dependent cloud processes are predominantly responsible for the formation of raindrops. Therefore, the temporal variation of the sedimentation flux of raindrops shown in Figure 14 provides concrete evidences to confirm that the activity of ice-dependent cloud processes in the air has great impacts on the variation of the rainfall on the ground.

What has revealed in the study regarding the active ice-dependent processes distinguishes the Meiyu frontal rainstorms from other rainstorms occurred in other regions (Cui et al., 2007; Huang & Cui, 2015). Two main pathways responsible for the generation of raindrops are revealed in previous study for the inland rainstorms occurring near the eastern slope of Tibetan Plateau (Huang & Cui, 2015). One pathway is water vapor condensing into cloud liquid water first, followed by the accretion process to form rainwater. The other pathway is water vapor condensing into cloud liquid water at the beginning, followed by freezing accretion processes to form graupel instead of rainwater, and finally melting into rainwater. This means that the warm cloud processes (first pathway) and the ice cloud processes (second pathway) coexist in this type of rainstorm and possess nearly equivalent importance for the formation of raindrops. Similar characteristics are found in the tropical rainstorms. The warm cloud processes and ice cloud processes contribute 60% and 40% to the source of raindrops, respectively, in the stratiform cloud regions, while the proportions for the two pathways are adjusted to 85% and 15%, respectively, in convective cloud regions (Cui et al., 2007). Different from these two types of rainstorms, the ice-dependent cloud processes play much more significant role in the formation of raindrops in the Meiyu frontal rainstorm, yet the role of the warm cloud processes can be set aside, especially in the heavy rainfall region (Ni & Zhou, 2006; Wang & Yang, 2003; Zhang et al., 2009). Despite that the hydrometeor budget analysis of Meiyu frontal rainstorm here revealed some similar characteristics with previous study, to be specific, the melting of ice phase hydrometeors is the major source term of the raindrops, which is discovered in both previous and present study, while the present study innovatively discovered a new conversion pathway for the formation of the major ice phase hydrometeors. According to the previous study, it is revealed that the accretion processes between cloud water and ice-phase hydrometeors (i.e., Route 3 shown in Figure 14) and the sublimation processes from water vapor to cloud ice followed by rime growth (i.e., Route 1 shown in Figure 14) are the only major conversion pathways for the formation of ice phase hydrometeors (Wang & Yang, 2003; Zhang et al., 2009). Actually, exception for these ones, the

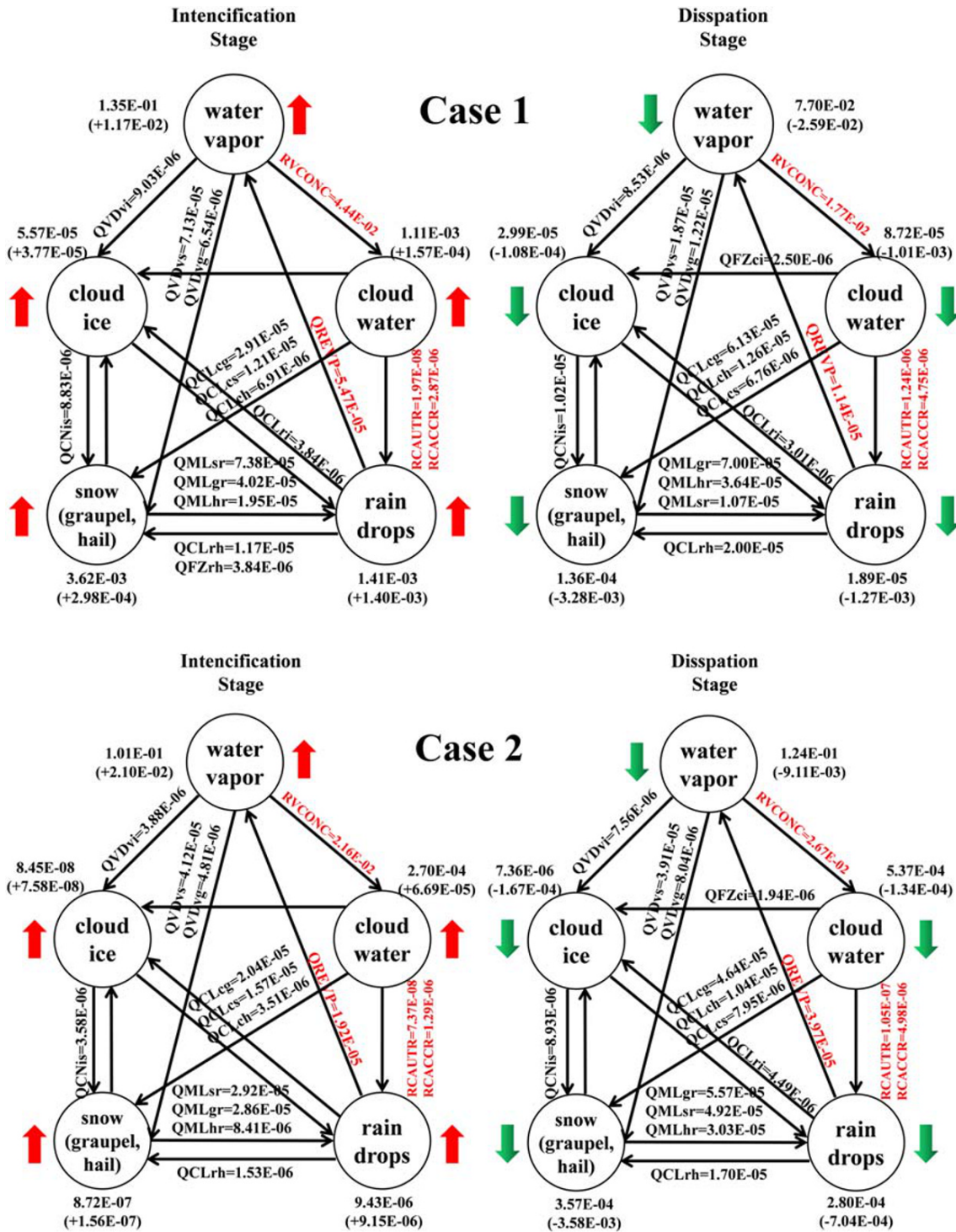


Figure 12. The schematic diagram for the hydrometeor budget among the whole species of hydrometeors for Case 1 (top) and Case 2 (bottom) (the red arrows denote positive trend, the green arrows denote negative trend, the values associated with the budget terms represent the temporal averaged hydrometeors path, unit: $\text{kg}/(\text{m}^2 \cdot \text{h})$, while the values associated with different hydrometeors represent the relative change of the hydrometeors path within the specified time span, unit: kg/m^2).

present study confirms that the direct sublimation processes from water vapor to graupel and snow (i.e., Route 2 shown in Figure 14) are another important source term of the major ice phase hydrometeors that cannot be ignored.

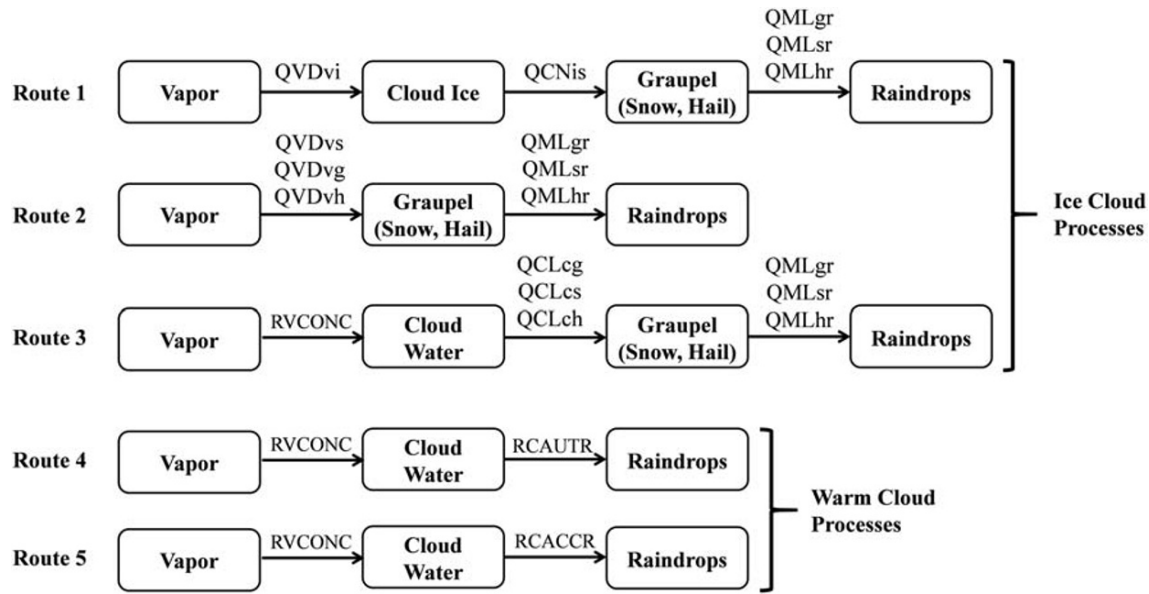


Figure 13. The schematic diagram of the routes (Routes 1 to 3 refer to the ice cloud processes and Routes 4 to 5 refer to the warm cloud processes) of microphysical processes responsible for the formation of raindrops in the Meiyu frontal rainstorms.

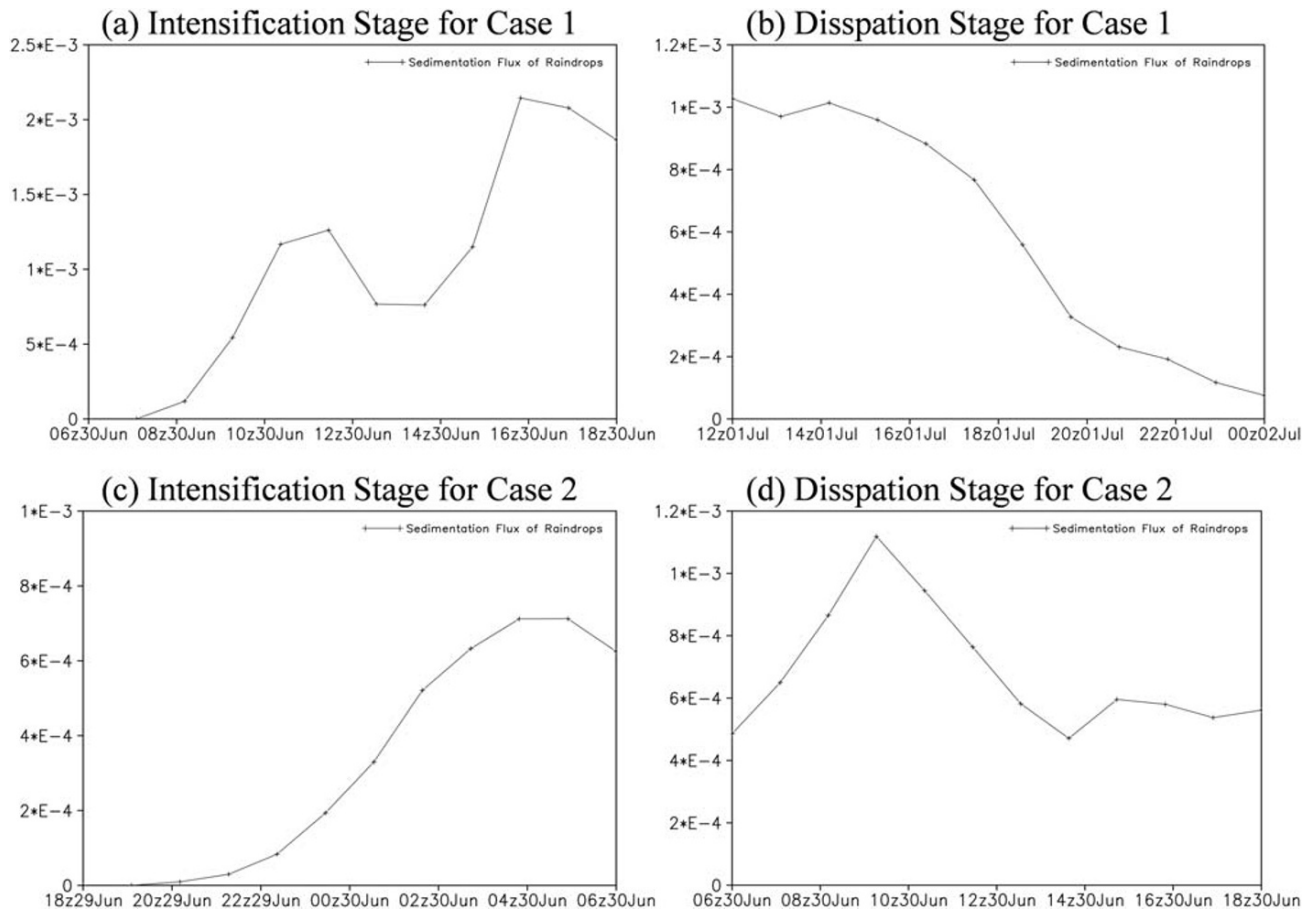


Figure 14. The variation of the spatiotemporal averaged sedimentation flux of raindrops in the intensification stage (a and c) and the dissipation stage (b and d) for Case 1 (top) and Case 2 (bottom) (x axis denotes the time, y axis denotes the sedimentation flux, unit: $m^3/(m^2 \cdot s)$).

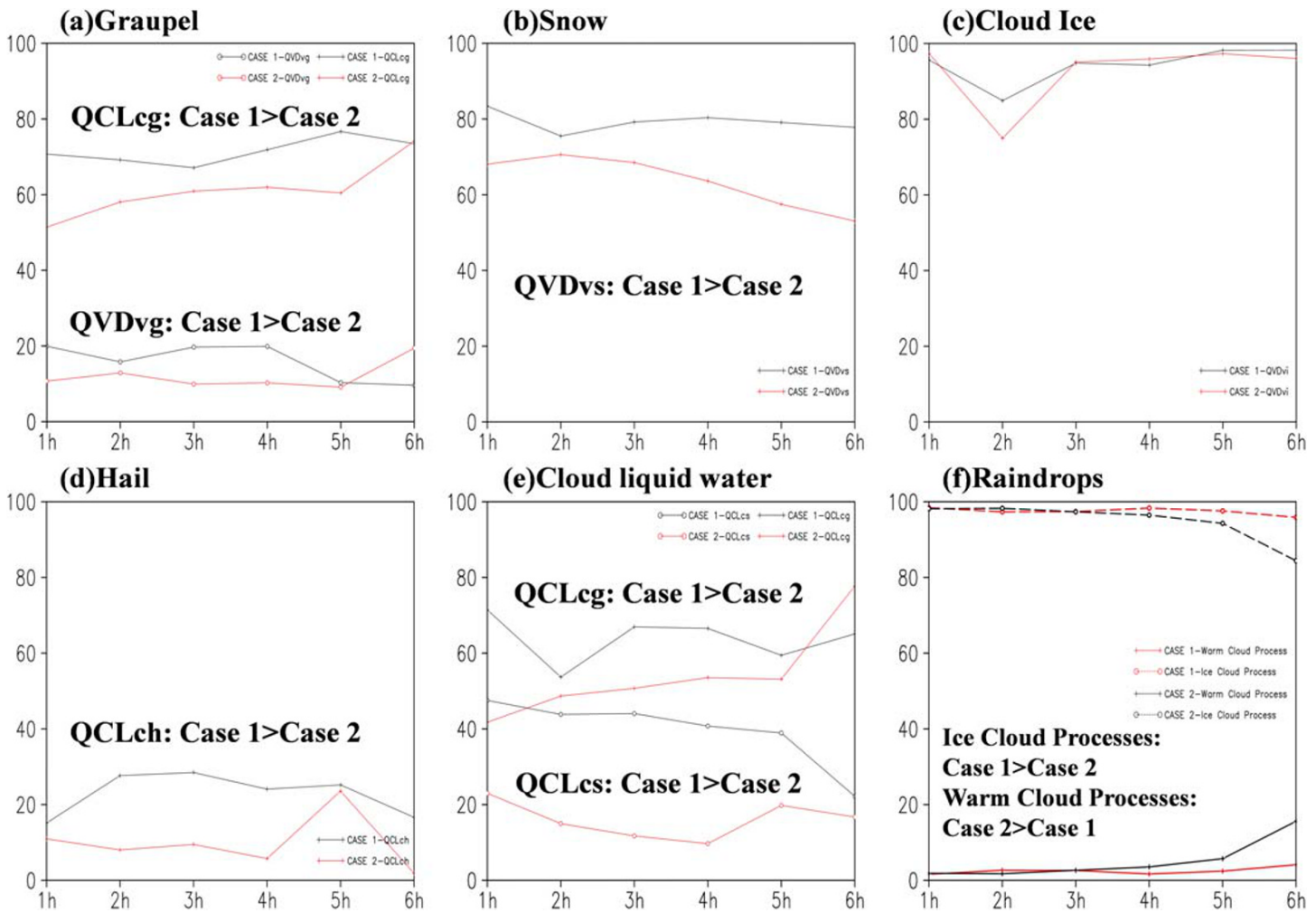


Figure 15. The contrast of the contribution rate (black solid line for Case 1, red solid line for Case 2) of the dominant budget terms to the formation of the associated hydrometeors ((a) graupel, (b) snow, (c) cloud ice, (d) hail, (e) cloud liquid water, (f) raindrops) between Case 1 and Case 2 (x axis denotes the contrasting time span defined as the relative time, y axis denotes the percentage of the contribution rate, unit: %).

5.4. The Quantitative Contrast of the Activity Level of Ice-Dependent Cloud Processes Between Case 1 and Case 2

As stated above, the fairly similar conversion pathways among different species of hydrometeors for the formation of raindrops are revealed in both Case 1 and Case 2, and the budget characteristics of those ice-dependent cloud processes show some discrepancies in the meanwhile, especially in the intensification stage, thus a diagnosed parameter called contribution rate (CR) is proposed for a quantitative measurement on the exact difference of the budget characteristics between Case 1 and Case 2. The quantity of CR is defined as the proportion of one single budget term or the totality of several budget terms in the totality of all budget terms of their associated hydrometeors regarding the contribution to the growth or consumption processes of the associated hydrometeors. Considering the more remarkable discrepancies of hydrometeors budget characteristics between Case 1 and Case 2 in the intensification stage than the dissipation stage, and the more steady increase of precipitation in the second half of time slot than the first half of time slot during the intensification stage, thus the time slot selected out for detailed contrast is focused the period from 13z30Jun2016 to 18z30Jun2016 in Case 1 and the period from 01z30Jun2018 to 06z30Jun2018 in Case 2, respectively. The temporal variation of CR for the dominant terms in the specified time slot is shown in Figure 15. It is clearly demonstrated that the dominant ice-dependent cloud microphysical processes like QVDvs, QVDvg have a notably higher contribution rate for the formation of snow and graupel in Case 1 than that in Case 2. The

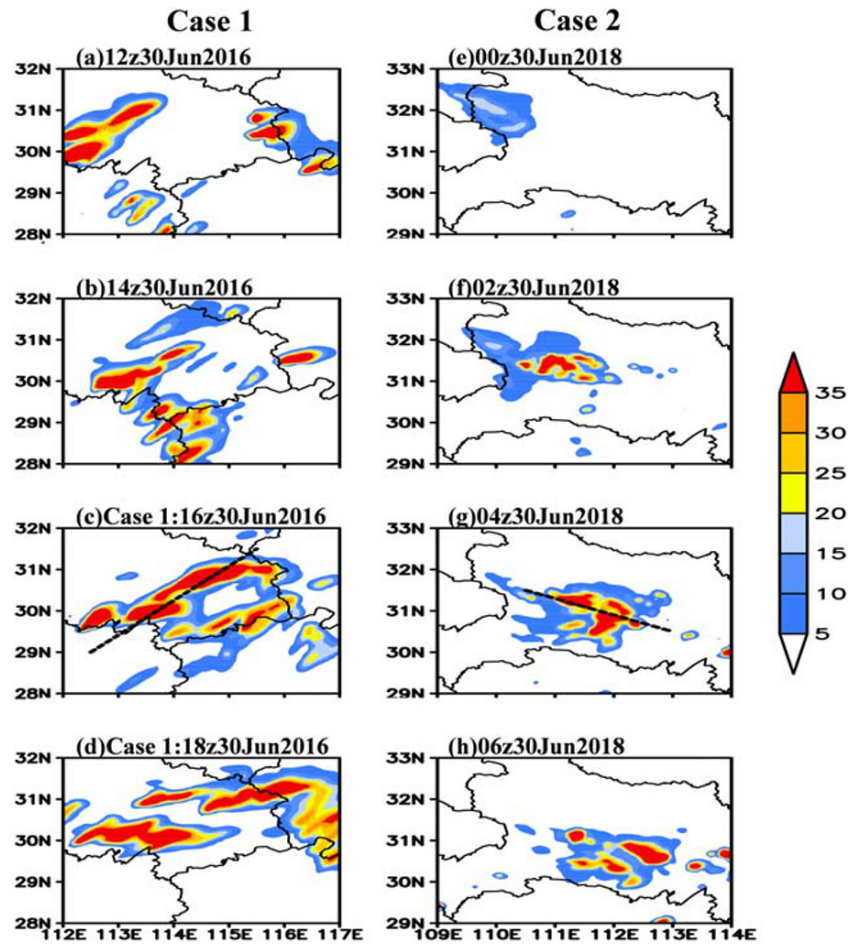


Figure 16. The distribution of the accumulated precipitation (shaded color, unit: mm) within 2 hr during the intensification stage for Case 1 (a-d) and Case 2 (e-h) (the dotted lines in panels (c) and (f) mark out the location of the profile for further analysis in the following).

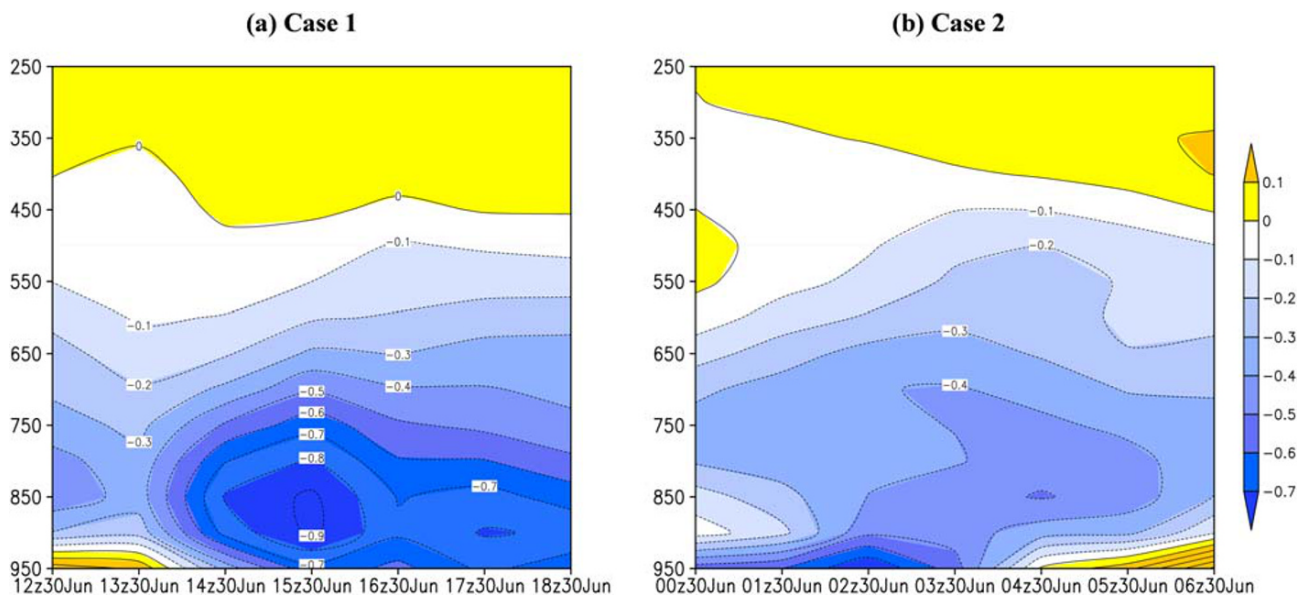


Figure 17. The variation of the regional-averaged (marked with black rectangles in Figure 7) water vapor flux divergence (shaded color, unit: $10^4 \text{kg}/(\text{s} \cdot \text{m}^2 \cdot \text{hPa})$) with the intensification stage for Case 1 (a) and Case 2 (b).

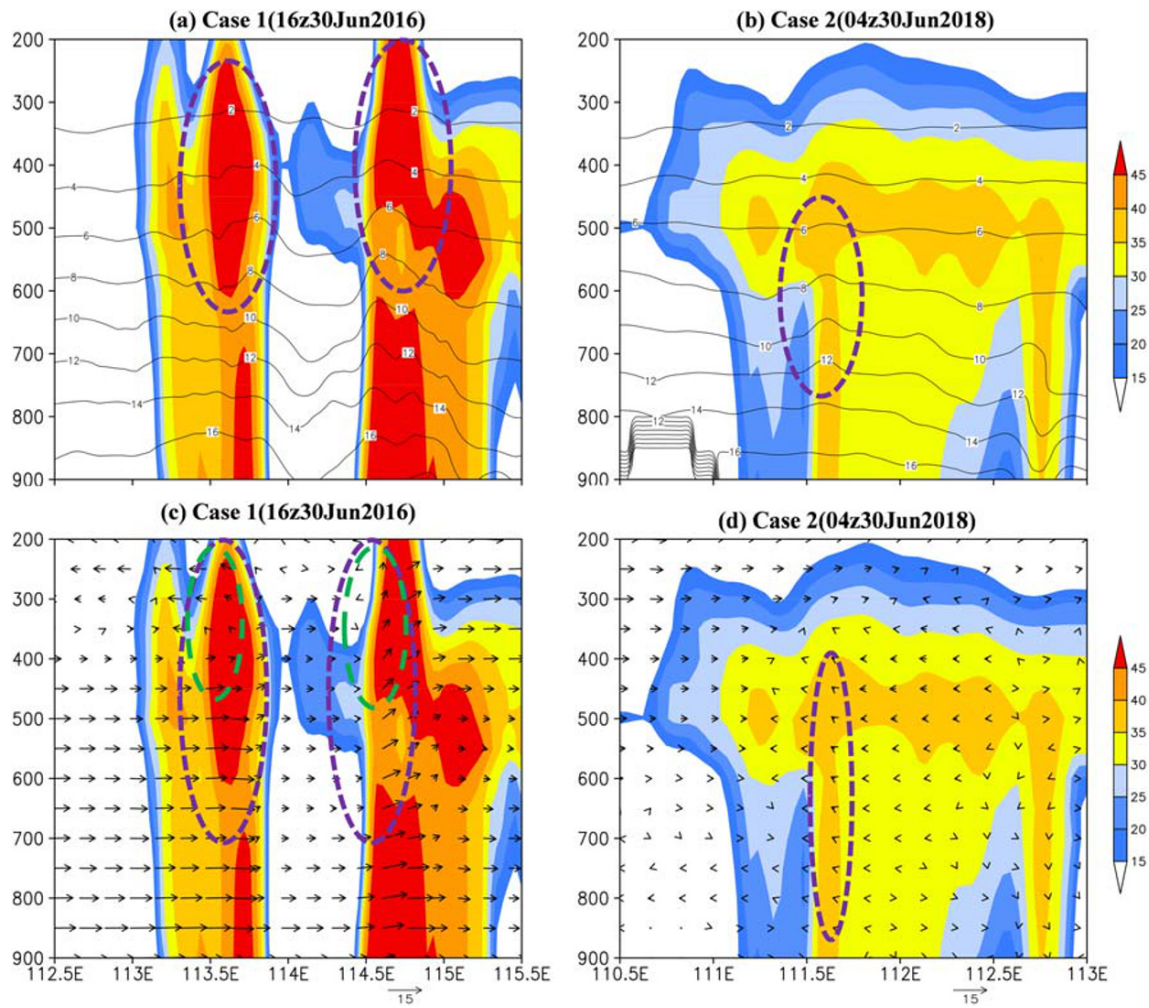


Figure 18. The profile (marked with dotted lines in Figure 16) of the radar reflectivity (shaded color, unit: dbz), specific humidity (solid lines in (a) and (b), unit: g/kg), and the wind velocity (arrows in (c) and (d), unit: m/s) based on WRF simulation for Case 1 (left) and Case 2 (right) at specified moment.

other dominant ice-dependent cloud microphysical processes like QCLch, QCLcg, QCLcs also have a notably higher contribution rate for the formation of the associated ice phase hydrometeors. Aiming to reveal the differences of the activity level of ice-dependent cloud processes targeted for the formation of raindrops, the CR of the ice cloud processes (the totality of QMLsr, QMLgr, QMLhr, QMLgr, QCLsr) and the warm cloud processes (the totality of RCAUTR, RCACCR) for Case 1 and Case 2 are calculated out and shown in Figure 15f. The result shows that the ice cloud processes have a slightly higher CR in Case 1 than that in Case 2, and the warm cloud processes have a slightly lower contribution rate in Case 1 than that in Case 2 accordingly. Besides, the enormous gap of CR between the ice cloud processes and the warm cloud processes targeted for the formation of raindrops revealed in both Case 1 and Case 2 reconfirms the greater importance of ice cloud processes compared to the warm cloud processes in affecting the variation of precipitation. Based on the integrative analysis of the contrast results regarding the dominant budget terms, it can be naturally concluded that the ice-dependent microphysical processes in Case 1 are more active than that in Case 2.

5.5. The Mechanism of how the Differences of Atmospheric Circulation Result in the Discrepancy of the Activity Level of Ice-Dependent Cloud Processes

The same time spans are selected out from the intensification stage in Case 1 and Case 2, accounting for the active ice-dependent cloud processes with the steady increase of precipitation (shown in Figure 16). Considering the special relevance of the adequate supply of water vapor to the occurrence of heavy rainfall and the cloud microphysical processes, the temporal variations of regional-averaged water vapor flux

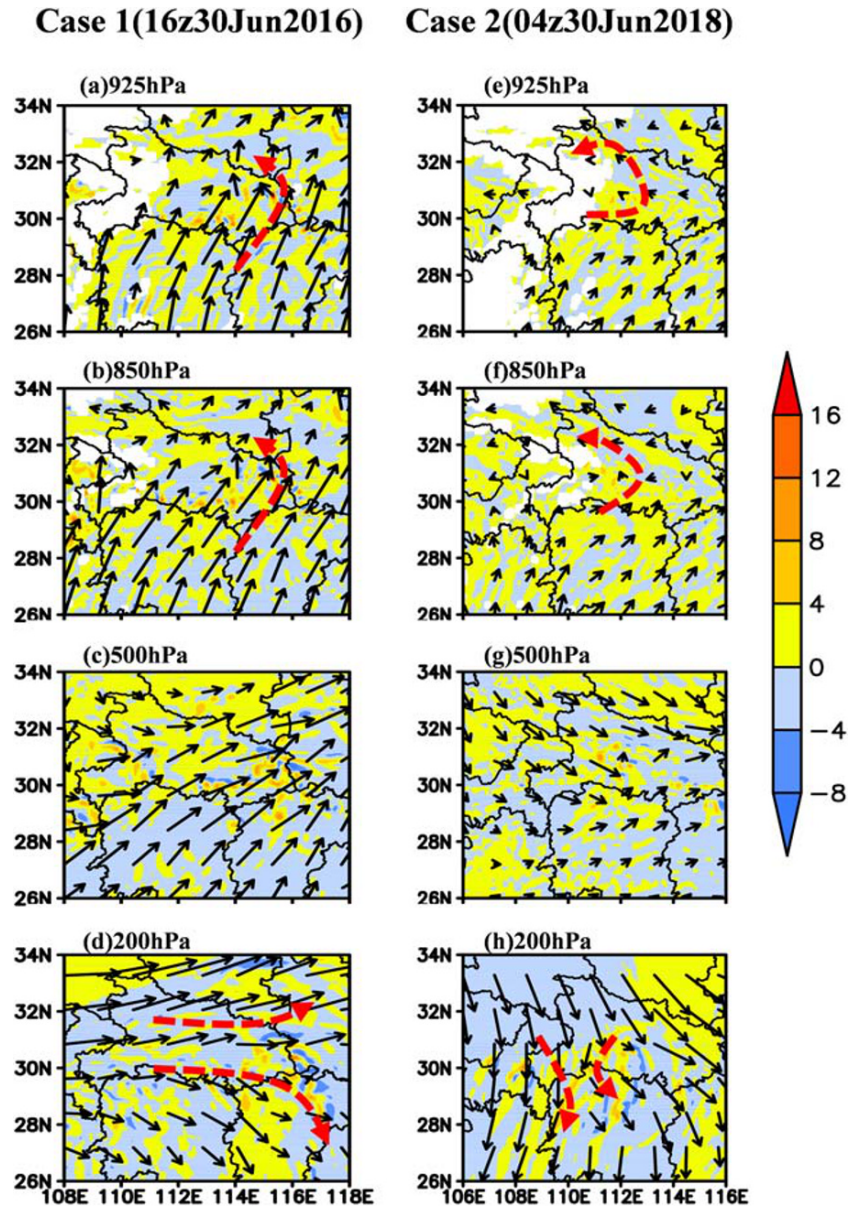


Figure 19. The wind (black arrows, unit: m/s) and relative vorticity (shaded, unit: 10^5 s^{-1}) on different isobaric surfaces (925, 850, 500, 200 hPa) for Case 1 (a–d) and Case 2 (e–h) at a specified moment (the red bold arrows mark out the anomalous distribution of wind).

divergence for Case 1 and Case 2 are presented in Figure 17. It is revealed that the enhancement of convergence of water vapor flux in lower troposphere (below 700 hPa) arises a little earlier than the precipitation intensity for both Case 1 and Case 2. More importantly, the convergence intensity of water vapor flux in Case 1 exceeds over that one in Case 2 remarkably. For deepening understanding of the dynamic and thermal atmospheric conditions determined by the atmospheric circulation pattern, two cross-sections (location marked with black dotted lines in Figures 16c and 16g) through the maximal rainfall center derived from Case 1 and Case 2 are picked out for further contrast. It is clearly shown that the convection intensity over the maximum rainfall center in Case 1 is significantly stronger than that in Case 2 in Figure 18. Additionally, the updraft accompanied with the strong radar reflectivity nearby is also stronger in Case 1 than that in Case 2 (marked with purple ellipse in Figures 18c and 18d). Simultaneously, it is also observed that the specific humidity in the middle and upper troposphere for Case 1 is greater than that in Case 2 within the severe convection area, while the gap of the specific

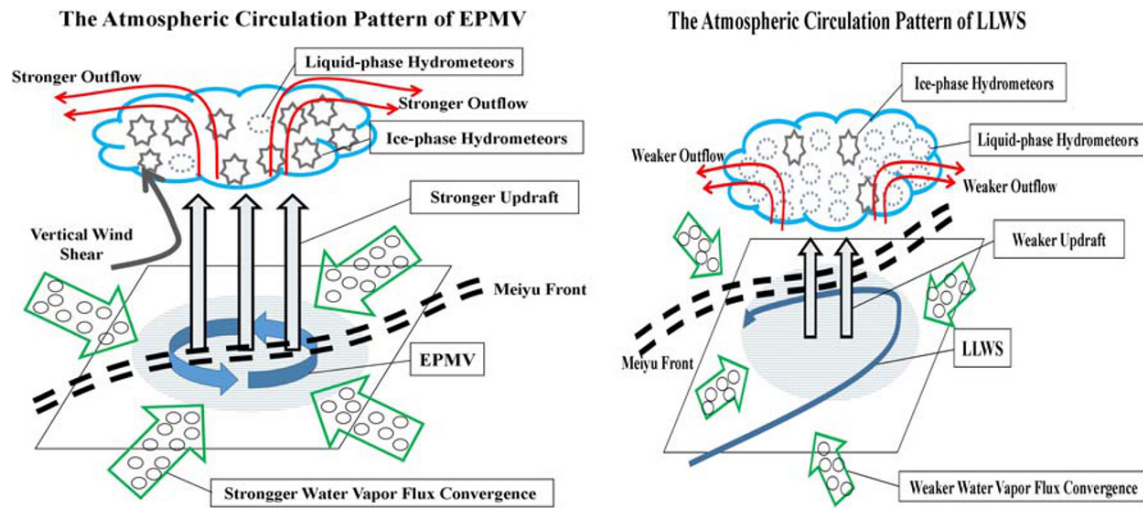


Figure 20. The schematic diagram of the concept model on how different atmospheric circulation patterns (left for EPMV pattern, right for LLWS pattern) result in different activity level of the ice-dependent cloud processes.

humidity between the two cases is smaller outside the severe convection area. Moreover, the vertical wind shear (marked with green ellipse in Figure 18c) in the upper troposphere is only observed in Case 1, which is important to the maintenance of convective clouds (Takeda, 1971). Furthermore, the more favorable circulation collocation in lower and upper level is shown in Figure 19 (i.e., the more intensive wind convergence in lower troposphere and the wider wind divergence in upper troposphere in Case 1 than those in Case 2), which is advantageous for the persistence of the greater convergence of water vapor flux and the stronger updraft.

The above analysis reveals that the atmospheric conditions determined by the two different atmospheric circulation patterns (one case is dominated by EPMV and the other case is dominated by LLWS) show distinct features. Taking all the above distinct features into integrative analysis, then a concept model on how the differences of the circulation patterns result in the discrepancies of the activity level of the ice-dependent cloud processes is effectively built. The concept model explicitly explained that the better dynamic and thermal conditions in Case 1 listed in the following are mainly responsible for the more active ice-dependent cloud processes compared Case 2. Specially speaking, EPMV concentrates more water vapor within the heavy rainfall region by the greater wind convergence in the lower troposphere, then the more favorable collocation of the atmospheric circulation in the lower and upper troposphere spurs the strengthening of the updraft. Consequently, the stronger severe convection is activated by the latent heat release of the more supply of water vapor transported by updraft in the middle troposphere, then a stable convective airflow cylinder is formed to transport more underutilized water vapor and water droplets condensed from water vapor in the middle troposphere to the upper troposphere. Simultaneously, the stronger outflow forced by the vertical shear or the stronger divergent circulation in the upper troposphere stimulates the vertical transportation by updraft extending to higher level. Thus, the integrative effect of the overall dynamic and thermal dynamic conditions results in more water vapor and water droplets being transported to the freezing layer where active ice-dependent cloud processes take place. While those conditions listed above in Case 2 are inferior to Case 1 in sustaining the transportation of water vapor, which leads to the discrepancy of the activity level of ice-dependent processes. Finally, a schematic diagram of the concept model (shown in Figure 20) is proposed for an intuitive demonstration of the above mechanism.

Generally speaking, although the schematic diagram derived from our study shares some similarities with previous study drawn by Zhao et al. (2004) who built a convective cloud cluster model to explain how the meso- γ convective cells is generated in the atmospheric circulation dominated by Meiyu front and how the in-cloud particles vertically distributed under the impact of convective cell, yet some discrepancies between these two different schematic diagrams should be paid more attention to. Different from what is revealed by Zhao, the inflow to trigger the severe convection in the present study is mainly forced by the

low-level wind convergence dominated by the local mesoscale system, while Zhao thought the synoptic scale of LLJ (Low Level Jet) has the predominant effect on the inflow to trigger the severe convection. Due to the important role of the inflow affirmed in the present study and previous study, thus the discrepancy of inflow intensity determined by the different circulation patterns can be regarded as one of key factors to explain the differences the activity level of ice-dependent cloud processes in the case of EPMV and LLWS.

6. Conclusion and Discussion

Since Meiyu frontal rainstorms pose major threats to human lives, property, and socioeconomic development via a high possibility of causing disastrous flooding in summer, further study concerning the occurrence and development mechanisms of heavy precipitation, especially the relevant cloud microphysical processes, is in great demand. Thus, two representative cases of Meiyu frontal rainstorms associated with totally different atmospheric circulation patterns were selected out to study the correlation between the cloud microphysical processes and the evolution of the heavy rainfall. Details concerning the cloud microphysical processes relevant to the two different types of Meiyu frontal rainstorms are revealed through the analysis of the hydrometeor budget. The main findings are listed in the following: Observation of background circulations shows that the atmospheric circulation patterns in Case 1 and Case 2 are totally different. Case 1 is characterized by the coupling between the EPMV and the Meiyu front, which occurred during 30th June and 2nd July in 2016, while Case 2 (captured during the 2018 IMFRE campaign) is dominated by the interaction between the LLWS and the Meiyu front, which occurred during 29th June and 30th June in 2018. The atmospheric circulation patterns determine the two cases belonging to two different types of Meiyu frontal rainstorms based on the previous classification criteria. The evolution stages for both Case 1 and Case 2 are divided into two stages (i.e., intensification stage and dissipation stage). The two cases share similar input and output terms of the hydrometeor budget system revealed by the hydrometeor budget diagnosis. These terms include the deposition from the water vapor to the ice phase hydrometeors (i.e., graupel, snow, hail, cloud ice), the accretion from the cloud liquid water to the ice phase hydrometeors in the upper troposphere, and the melting of the ice phase hydrometeors into the raindrops in the mid-lower troposphere. However, the significant difference of the hydrometeor budget between Case 1 and Case 2 lies in the melting of ice phase hydrometeors to raindrops. To be specific, the melting of snow contributes more to the formation of raindrops compared to graupel during the intensification stage in Case 2, while the melting of graupel contributes more during the intensification stage in Case 1. The possible causes of the opposite change may be ascribed to the more remarkable reinforcement of the accretion from cloud liquid water to graupel (i.e., QCLG), and then promoting the melting of graupel to raindrops indirectly. Then microphysical flowchart among different species of hydrometeors is formed based on the overall hydrometeor budget analysis. Subsequently, three major ice cloud conversion pathways and two minor warm cloud conversion pathways responsible for the formation of raindrops are identified. The major routes of ice cloud processes can be regarded as the constitution of those ice-dependent cloud microphysical processes (primarily including the deposition processes and the accretion processes) in the upper troposphere and those melting processes in the mid-lower troposphere roughly, while the minor routes of warm cloud processes can be regarded as those liquid water conversion processes without phase change (primarily including the auto conversion processes, the accretion processes, the condensation or evaporation processes between cloud water and raindrops). The detailed contrast of CR with respect to the dominant budget terms of different hydrometeors confirms more active ice-dependent cloud processes in Case 1 than that in Case 2. These findings demonstrate that the Meiyu frontal rainstorms actually have active ice-dependent cloud processes, but the activity level of ice-dependent cloud processes differs with the change of the atmospheric circulation patterns. Then a question on what's the inner-connection between the ice-dependent cloud processes and the atmospheric circulation pattern is brought up naturally. Further analysis figures out that the discrepancies of those dynamic and thermodynamic atmospheric conditions determined by the atmospheric circulation pattern are mainly responsible for the differences of the activity level of ice-dependent cloud processes. Finally, a schematic diagram of concept model (shown in Figure 20) based on the refinement of the above conclusions presents an explicit demonstration of how the differences of atmospheric circulation patterns result in the differences of the activity level of ice-dependent cloud processes.

Despite several new findings concerning the cloud microphysical processes are presented here, yet the present analysis has several limitations. First and foremost, the analysis is based on only two

representative cases and more events are needed to further enhance the robustness of the conclusions. Second, more observations are needed to warrant a quantitative validation of the WRF microphysics in Meiyu rainstorms when the observation targeted for the microphysical processes in Meiyu rainstorms are improved in future. Finally, a rough explanation to why Case 1 leads more active ice-dependent cloud processes than Case 2 is just based on the diagnosis of some dynamic and thermal dynamic conditions associated with atmospheric circulation, the details of how these conditions affect the intermediate conversion processes along the pathway responsible for the formation of ice phase hydrometeors also need further study. Therefore, better simulations and predictions of heavy Meiyu rainfall demand not only continued observing and modeling efforts, but also more in-depth research relevant to the ice-dependent cloud processes.

Data Availability Statement

The original data used in the paper are available from the RDA's website (<https://rda.ucar.edu>) in data set number ds083.2. The FY-2 series stationary satellite data were downloaded from National Satellite Meteorological Center's website (<http://satellite.nsmc.org.cn>). The CMORPH hourly fusion precipitation data were downloaded from the National Meteorological Information Center's website (<http://data.cma.cn>).

Acknowledgments

This work was supported jointly by the National Natural Science Foundation of China (grant 41620104009, 91637211, and 41975058), the National Key R&D Program of China (grant 2018YFC1507200), the Science and Technology Foundation of Hubei Meteorological Bureau (grant 2017Y03), the National Science Foundation Climate and Large-Scale Dynamics (CLD) program (grant AGS-1354402, AGS-1445956), and the National Oceanic and Atmospheric Administration through award (grant NA16NWS4680013). The authors are grateful to three anonymous reviewers for their helpful comments.

References

- Albers, S. C., McGinley, J. A., & Birkenheuer, D. L. (1996). The local analysis and prediction system (LAPS): Analyses of clouds, precipitation, and temperature. *Weather and Forecasting*, *11*(3), 273–287. [https://doi.org/10.1175/1520-0434\(1996\)011<0273:TLAAPS>2.0.CO;2](https://doi.org/10.1175/1520-0434(1996)011<0273:TLAAPS>2.0.CO;2)
- Birkenheuer, D. L. (1999). The effect of using digital satellite imagery in the LAPS moisture analysis. *Weather and Forecasting*, *14*(5), 782–788. [https://doi.org/10.1175/1520-0434\(1999\)014<0782:TEOUDS>2.0.CO;2](https://doi.org/10.1175/1520-0434(1999)014<0782:TEOUDS>2.0.CO;2)
- Birkenheuer, D. L. (2001). Utilizing variational methods to incorporate a variety of satellite data in the LAPS moisture analysis. Preprints, 11th Conf. on Satellite Meteorology and Oceanography, Madison, WI: Amer. Meteor. Soc.
- Cui, X., Zhou, Y., & Li, X. (2007). Cloud microphysical properties in tropical convective and stratiform regions. *Meteorology and Atmospheric Physics*, *98*(1–2), 1–11. <https://doi.org/10.1007/s00703-006-0228-1>
- Dudhia, J. (1989). Numerical study of convection observed during the winter monsoon experiment using a mesoscale two-dimensional mode. *Journal of the Atmospheric Sciences*, *46*(20), 3077–3107. [https://doi.org/10.1175/1520-0469\(1989\)046<3077:NSOCOD>2.0.CO;2](https://doi.org/10.1175/1520-0469(1989)046<3077:NSOCOD>2.0.CO;2)
- Fernandez, G. S., Wang, P. K., & Gascon, E. (2016). Latent cooling and microphysics effects in deep convection. *Atmospheric Research*, *180*, 189–199. <https://doi.org/10.1016/j.atmosres.2016.05.022>
- Grabowski, W., Morrison, H., Shima, S., & Abade, G. C. (2018). Modeling of cloud microphysics: Can we do better? *Bulletin of the American Meteorological Society*, *100*(4), 655–672. <https://doi.org/10.1175/BAMS-D-18-0005.1>
- Hiemstra, C. A., Liston, G. E., Pielke, R. A., & Birkenheuer, D. L. (2006). Comparing local analysis and prediction system (LAPS) assimilation with independent observations. *Weather and Forecasting*, *21*, 1020–1040.
- Hong, S. Y., Noh, Y., & Dudhia, J. (2006). A new vertical diffusion package with an explicit treatment of entrainment processes. *Monthly Weather Review*, *134*(9), 2314–2341.
- Huang, Y. J., & Cui, X. P. (2015). Dominant cloud microphysical processes of a torrential rainfall event in Sichuan, China. *Advances in Atmospheric Sciences*, *32*(3), 389–400. <https://doi.org/10.1007/s00376-014-4066-7>
- Jiang, H. L., Steve, A., Xie, Y. F., Zoltan, T., Isidora, J., Michael, S., et al. (2015). Real-time applications of the variational version of the local analysis and prediction system (vLAPS). *Bulletin of the American Meteorological Society*, *96*(12), 2045–2057. <https://doi.org/10.1175/BAMS-D-13-00185.1>
- Jimenez, P. A., & Dudhia, J. (2012). A revised scheme for the WRF surface layer formulation. *Monthly Weather Review*, *140*(3), 898–918. <https://doi.org/10.1175/MWR-D-11-00056.1>
- Kenneth, L. K., & Liu, C. M. (1990). Theoretical study of the cloud physics of Mei-yu. *Journal of Geophysical Research*, *95*(D12), 20417–20426.
- Li, H., Cui, C., & Wang, Z. (2009). Scientific designs, functions and applications of LAPS. *Torrential Rain and Disasters*, *28*, 64–70. (in Chinese)
- Milbrandt, J. A., & Yau, M. K. (2005a). A multimoment bulk microphysics parameterization. Part I: Analysis of the role of the spectral shape parameter. *Journal of the Atmospheric Sciences*, *62*, 3051–3064.
- Milbrandt, J. A., & Yau, M. K. (2005b). A multimoment bulk microphysics parameterization. Part II: A proposed three moment closure and scheme description. *Journal of the Atmospheric Sciences*, *62*, 3065–3081.
- Milbrandt, J. A., & Yau, M. K. (2006). A multimoment bulk microphysics parameterization. Part IV: Sensitivity experiments. *Journal of the Atmospheric Sciences*, *63*, 3137–3159.
- Mlawer, E. J., Taubman, S. J., Brown, P. D., Taubman, S. J., Brown, P. D., Iacono, M. J., & Clough, S. A. (1997). Radiative transfer for inhomogeneous atmosphere: RRTM, a validated correlated-k model for the long wave. *Journal of Geophysical Research*, *102*(D14), 16663–16682. <https://doi.org/10.1029/97JD00237>
- Morrison, H., & Milbrandt, J. A. (2011). Comparison of two-moment bulk microphysics schemes in idealized supercell thunderstorm simulations. *Monthly Weather Review*, *139*(4), 1103–1130. <https://doi.org/10.1175/2010MWR3433.1>
- Ni, Y., & Zhou, X. (2006). Study on formation mechanisms of heavy rainfall within the Meiyu along the mid-lower Yangtze River and theories and methods of their detection and prediction. *Acta Meteorologica Sinica*, *20*(2), 191–208.
- Normura, M., Tsuboki, K., & Shinoda, T. (2012). Impact of sedimentation of cloud ice on cloud-top height and precipitation systems simulated by a cloud-resolving model. *Journal of the Meteorological Society of Japan*, *90*(5), 791–806. <https://doi.org/10.2151/jmsj.2012-514>

- Shen, Y., Zhao, P., Pan, Y., & Yu, J. (2014). A high spatiotemporal gauge-satellite merged precipitation analysis over China. *Journal of Geophysical Research: Atmospheres*, *119*, 3063–3075. <https://doi.org/10.1002/2013JD020686>
- Suzuki, K., Matsuo, M., Nakano, E., Shigeto, S., Yamaguchi, K., & Nakakita, E. (2014). Graupel in the different developing stages of Baiu monsoon clouds observed by vide sondes. *Atmospheric Research*, *142*, 100–110. <https://doi.org/10.1016/j.atmosres.2013.09.020>
- Takahashi, T. (2006). Precipitation mechanism in east Asian monsoon: Video study. *Journal of Geophysical Research*, *111*, D09202. <https://doi.org/10.1029/2005JD006268>
- Takahashi, T., & Keenan, T. D. (2004). Hydrometeor mass, number, and space charge distribution in a “Hector” squall line. *Journal of Geophysical Research*, *109*, D16208. <https://doi.org/10.1029/2004JD004667>
- Takahashi, T., Yamaguchi, N., & Tetsuya, K. (2001). Vide sonde observation of torrential rain during Baiu season. *Atmospheric Research*, *58*(3), 205–228. [https://doi.org/10.1016/S0169-8095\(01\)00083-7](https://doi.org/10.1016/S0169-8095(01)00083-7)
- Takeda, T. (1971). Numerical simulation of a precipitation convective cloud: The formation of a “long-lasting” cloud. *Journal of the Atmospheric Sciences*, *28*(3), 350–376.
- Tao, S. Y. (1980). *Heavy Rainfall of China* (). Beijing: Science Press.
- Wang, P., & Yang, J. (2003). Observation and numerical simulation of cloud physical processes associated with torrential rain of the Meiyu front. *Advances in Atmospheric Sciences*, *20*(1), 77–96. <https://doi.org/10.1007/BF03342052>
- Xu, K. M. (1995). Partitioning mass, heat, and moisture budget of explicitly simulated cumulus ensembles into convective and stratiform components. *Journal of the Atmospheric Sciences*, *52*(5), 551–573. [https://doi.org/10.1175/1520-0469\(1995\)052<0551:PMHAMB>2.0.CO;2](https://doi.org/10.1175/1520-0469(1995)052<0551:PMHAMB>2.0.CO;2)
- Zhang, M., & Zhang, D. L. (2012). Subkilometer simulation of a torrential-rain-producing mesoscale convective system in East China. Part I: Model verification and convective organization. *Monthly Weather Review*, *140*, 184–201.
- Zhang, X. L., Tao, S. Y., & Zhang, S. L. (2004). Three types of heavy rainstorms associated with the Meiyu front. *Chinese Journal of Atmospheric Sciences*, *28*(2), 187–205.
- Zhang, Y., Lei, H., Pan, X., Wang, C., & Xie, Y. (2009). Study on cloud micro-physical processes and precipitation formative mechanism of a mesoscale convective system in Meiyu front in June 2004. *Scientia Meteorologica Sinica*, *29*(4), 434–446. (in Chinese)
- Zhao, S., Tao, Z., Sun, J., & Bei, L. (2004). *Study on Mechanism for Rainstorm from the Meiyu Front over the Mid-Lower Yangtze Basin* (p. 282). Beijing: China Meteorological Press. (in Chinese)
- Zhou, Y. S., Gao, S. T., & Shen, S. S. P. (2004). A diagnostic study of formation and structures of the Meiyu front system over East Asia. *Journal of the Meteorological Society of Japan*, *82*(6), 1565–1576. <https://doi.org/10.2151/jmsj.82.1565>